

The Kinematics and Metallicity of the M31 Globular Cluster System

K. M. Perrett,¹ T. J. Bridges,² D. A. Hanes,¹ M. J. Irwin,³ J. P. Brodie,⁴ D. Carter,⁵
J. P. Huchra,⁶ and F. G. Watson²

ABSTRACT

With the ultimate aim of distinguishing between various models describing the formation of galaxy halos (e.g. radial or multi-phase collapse, random mergers), we have completed a spectroscopic study of the globular cluster system of M31. We present the results of deep, intermediate-resolution, fibre-optic spectroscopy of several hundred of the M31 globular clusters using the Wide Field Fibre Optic Spectrograph (WYFFOS) at the William Herschel Telescope in La Palma, Canary Islands. These observations have yielded precise radial velocities ($\pm 12 \text{ km s}^{-1}$) and metallicities ($\pm 0.26 \text{ dex}$) for over 200 members of the M31 globular cluster population out to a radius of 1.5 degrees from the galaxy center. Many of these clusters have no previous published radial velocity or $[\text{Fe}/\text{H}]$ estimates, and the remainder typically represent significant improvements over earlier determinations. We present analyses of the spatial, kinematic and metal abundance properties of the M31 globular clusters. We find that the abundance distribution of the cluster system is consistent with a bimodal distribution with peaks at $[\text{Fe}/\text{H}] \sim -1.4$ and -0.5 . The metal-rich clusters demonstrate a centrally concentrated spatial distribution with a high rotation amplitude, although this population does not appear significantly flattened and is consistent with a bulge population. The metal-poor clusters tend to be less spatially concentrated and are also found to have a strong rotation signature.

Subject headings: galaxy formation, globular cluster systems, M31, spectroscopy, kinematics

1. Introduction

The mechanisms involved in galaxy formation remain one of the major unsolved problems in astronomy. Over the past several decades, various groups have proposed a range of models which endeavor to explain the observed properties of galaxies and their globular cluster systems (GCSs). One

early formation model from Eggen, Lynden-Bell, & Sandage (1962) argues for a single, large-scale collapse of material to form galactic bodies such as the Milky Way. A principal competing model maintains that formation has occurred through random mergers of fragmented gas clouds over the course of billions of years, implying a hierarchical origin (Searle & Zinn 1978; Cole et al. 2000). In order to interpret the bimodality seen in the globular cluster metallicity and color distributions of many galaxies (Ashman & Zepf 1998), additional scenarios have been put forth such as multiphase *in situ* formation (Forbes, Brodie, & Grillmair 1997), major mergers (Zepf & Ashman 1993) and tidal stripping/capture (Côté, Marzke, & West 1998).

Support for the idea that the Milky Way halo formed in a hierarchical or episodic manner arises from the lack of a significant abundance gradient throughout the entire halo globular cluster pop-

¹Department of Physics, Queen's University, Kingston, ON K7L 3N6, Canada

²Anglo-Australian Observatory, Epping, NSW, 1710 Australia

³Institute of Astronomy, Cambridge University, Cambridge CB3 0HA, England, UK

⁴UCO/Lick Observatory, University of California at Santa Cruz, Santa Cruz, CA 95064, USA

⁵Liverpool John Moores University, Twelve Quays House, Egerton Wharf, Birkenhead, CH41 1LD, England

⁶Harvard-Smithsonian Center for Astrophysics, 60 Garden Street, Cambridge, MA 02138, USA

ulation (Parmentier et al. 2000), a notable decrease in the radial component of the velocity ellipsoid of the stellar halo beyond the solar circle (Sommer-Larsen et al. 1997), and the detection of a possible spread in cluster and stellar ages within the outer halo (Sarajedini, Chaboyer, & Demarque 1997; Rosenberg et al. 1999; Stetson et al. 1999). In addition, some studies have uncovered evidence of kinematic and chemical sub-clustering within the globular cluster population of the Andromeda galaxy which may point to accretion remnants (Ashman & Bird 1993; Saito & Iye 2000). However, it is possible that some degree of fragmentation might arise in an infall scenario due to thermal and gravitational instabilities within the collapsing proto-galactic gas cloud. A better understanding of the fragment properties including chronology, chemistry and, in particular, kinematics would help us to identify the origin of sub-clustering and to differentiate between the various formation models.

It has been noted often that globular clusters (GCs) provide us with ideal probes of galaxy structure and formation mechanisms. As the oldest galactic stellar systems, globular clusters hold the key to uncovering the formation record of their host environments. Correlations between chemical content (which points to chronology) and the kinematics of globular clusters allow us to investigate the early formative stages of a galaxy and, to some extent, probe its ongoing evolution.

The M31 globular cluster system provides an obvious and desirable target of observation: (i) its proximity makes it the most accessible large system outside of the Milky Way; (ii) with $\gtrsim 435$ confirmed candidate members (Barmby et al. 2000), the M31 GCS is sufficiently populous that it provides a statistically significant sample size; (iii) unlike the Milky Way GCS, the M31 population can be observed over the full extent of the galaxy with less severe effects of line-of-sight contamination; (iv) all of the M31 clusters lie at essentially the same distance, and thus are not subject to such large individual distance uncertainties as are the Milky Way globulars. However, the proximity of M31 introduces certain issues of contamination within the cluster sample, such as a difficulty in distinguishing between GC candidates and star-forming regions in many photometric surveys. Furthermore, faint globular clusters can easily be

missed against the bright galaxy background.

Previous studies of the Milky Way and M31 globular cluster systems have revealed that these two populations exhibit some remarkable similarities. Zinn (1985) found that the Galactic GCS demonstrated clear evidence for bimodality in its metallicity distribution, and proposed that it could be considered as two distinct subsystems: a flattened, metal-rich, rapidly rotating, kinematically cold disk system, and a spherical, metal-poor halo with lower net rotation and higher velocity dispersion. Signs of bimodality have been found in the M31 metallicity distribution (Ashman & Bird 1993) and in metallicity-sensitive color distributions (Barmby et al. 2000). Separating the M31 clusters into metallicity sub-systems along the same lines as the Milky Way GCS, Huchra, Brodie, & Kent (1991) found that the metal-rich clusters within $R \sim 7'$ form a rapidly rotating ($100 - 200 \text{ km s}^{-1}$) disk-like system, whereas the metal-poor clusters within this radius exhibit no net rotation. Beyond this radius, they were unable to distinguish the metal-rich from metal-poor populations on the basis of kinematics. Later studies have provided additional evidence supporting the view that M31 has a rapidly rotating system of metal-rich globular clusters (Ashman & Bird 1993; Barmby et al. 2000).

Armandroff (1989) confirmed the presence of a modest metallicity gradient within the system of disk clusters in the Milky Way. In the first extensive spectroscopic survey of the M31 GCS, van den Bergh (1969) found no significant metallicity gradient with position but did report a wide range of abundances at any given radius. More recently, Huchra et al. (1982, 1991) and Sharov (1988) have shown that there is evidence for a weak but measurable metallicity gradient with projected radius in the M31 cluster system. A similar finding was reported by Barmby et al. (2000) based on their large sample of metal-sensitive colors. Huchra, Brodie, & Kent (1991) found a mean M31 GC metallicity of $[\text{Fe}/\text{H}] = -1.2$, slightly higher than that for the Milky Way.

There remains a lack of persuasive evidence that would allow us to distinguish between halo formation models — or indeed to suggest a clear hybrid of (or alternative to) the classical formation scenarios. It is clear that an extensive database of high-precision data for the kinematic and chem-

ical tracers of a large number of host galaxies is required in order to help solve this currently intractable problem of galaxy formation. Only then can the samples be examined for clear evidence of kinematic anomalies, metallicity gradients and sub-structure which, if present, may point to the formation and enrichment processes which have occurred in the galaxy. With this objective, we present spectroscopic results for $\gtrsim 200$ M31 cluster candidates, adding a large number of new observations to the database.

This paper will take the following form: Section 2 contains a description of the target selection and coordinate determinations. In Section 3, we provide a summary of the data acquisition and reduction procedure along with a description of the velocity and metallicity determinations. We incorporate these new results into the broader sample of available M31 cluster data to provide an analysis of the abundance distribution of the globular cluster system of our nearest large spiral galaxy neighbor in Section 4. In Section 5, we examine the kinematics of the cluster system and provide a mass estimate for the galaxy. A summary and discussion of the results of this study are presented in Section 6.

2. Target Selection and Coordinates

The list of targets was selected from the catalogue of Battistini et al. (1987), with some additional central targets from unpublished CCD photometry by J. Huchra. Cluster positions accurate to $0''.2$ were determined from Automatic Plate Measuring (APM) scans of deep photographic plates of a $6^\circ \times 6^\circ$ area around M31. The accuracy of the APM cluster coordinates represent a marked improvement over existing M31 GCS positions, which have typically been measured to the nearest arcsecond.

Galactocentric coordinates for the GCs were computed relative to an adopted M31 central position of $\alpha_0 = 00^h40^m00.1^s$, $\delta_0 = +40^\circ59'43''$ (B1950):

$$\begin{aligned} X &= C_1 \sin(PA) + C_2 \cos(PA) \\ Y &= -C_1 \cos(PA) + C_2 \sin(PA), \end{aligned} \quad (1)$$

where $C_1 = [\sin(\alpha - \alpha_0) \cos \delta]$ and $C_2 = [\sin \delta \cos \delta_0 - \cos(\alpha - \alpha_0) \cos \delta \sin \delta_0]$. The X coordinate represents the position along the major axis of the

galaxy increasing towards the north-east along the major axis. The Y coordinate is the distance from the major axis above and below the galactic plane, with positive values towards the north-west. The position angle (PA) of the major axis was taken to be 38° (Kent 1989).

Numerous groups have contributed to the identification of the globular cluster members of M31 (Hubble 1932; Vetešnik 1962; Sargent et al. 1977; Crampton et al. 1985; Battistini et al. 1980, 1987, 1993). The ultimate result of this combined effort is that most of the clusters are known by more than one name, a fact which has the potential to cause confusion. The letters preceding the identification number in the M31 cluster target names given hereafter indicate the relevant catalogue reference as provided in Table 1.

3. The WYFFOS Data

The data for this study were obtained at the William Herschel 4.2 m telescope⁷ (WHT) in La Palma, Canary Islands, during the nights of November 3 to 6, 1996. The WYFFOS Wide Field Fibre Optic Spectrograph (Bridges 1998) was used with two gratings to provide a total spectral coverage of $\sim 3700 - 5600 \text{ \AA}$. The H2400B 2400-line grating yielded a dispersion of 0.8 \AA/pixel and a spectral resolution of 2.5 \AA over the range $3700 - 4500 \text{ \AA}$. This wavelength range was selected to investigate the CN feature at 3883 \AA , the H & K lines of calcium, $H\delta$, the CH G-band and the 4000 \AA continuum break. The R1200R 1200-line grating observations had a dispersion of 1.5 \AA/pixel and a resolution of 5.1 \AA over the spectral range $4400 - 5600 \text{ \AA}$ to add absorption features such as $H\beta$, the Mgb triplet and two iron lines near 5300 \AA .

Six different fibre configurations were selected to target a total of 288 globular cluster candidates over the full extent of the major axis of M31. An overlay of the WYFFOS target fields is shown superimposed on a Digitized Sky Survey image of the galaxy in Figure 1. A record of the observations is provided in Table 2, which includes the coordinates of the field centers, observation dates

⁷The William Herschel Telescope is operated on the island of La Palma by the Isaac Newton Group in the Spanish Observatorio del Roque de los Muchachos of the Instituto de Astrofísica de Canarias.

and exposure times. Regrettably, minor axis fields were not observed during this run due in part to a loss of time from poor weather.

Spectra of twilight flats, argon arc lamps, and velocity template stars were also obtained during the same nights of observation as the targets. The data reduction — including fibre throughput corrections, spectral extraction, sky subtraction and wavelength calibration — was accomplished using the `wyf_red` WYFFOS Multi-fiber IRAF⁸ package written by Jim Lewis. Ensemble median RMS values for the wavelength calibration were typically 0.02 – 0.08 Å for the H2400B grating images and 0.08 – 0.13 Å for the R1200R grating.

Most of the globular clusters in the M31 fields are superimposed on a relatively bright, non-uniform background of galaxy light. For the central WYFFOS fibre configurations, roughly 20 blank-sky fibres were arranged in a regular pattern across the 1° field to characterize the background intensity. The outer fields contained more dedicated sky fibres thanks to a lower density of targets in the area. Spectra obtained through the dedicated background sky fibres were averaged to form a composite sky spectrum which was then subtracted from each target. Attempting to match one or a few nearby sky fibres to each target spectrum (i.e. to associate the local sky level with each cluster) did not prove advantageous, since the resulting losses in signal-to-noise largely outweighed any gains in compensating for background variability even within the central fields. Examples of reduced spectra obtained using both gratings are shown in Figures 2 and 3 with the absorption features of interest labelled.

3.1. Radial Velocities

Radial velocities for the M31 globular clusters were calculated by performing standard Fourier cross-correlations of each target spectrum with the high signal-to-noise spectra of template stars of known velocity (Tonry & Davis 1979). Two spectra were acquired for each target, obtained using each of the R1200R and H2400B gratings. Two template stars, HD12029 (K2 giant) and HD23169 (G2 dwarf), were also observed during the run

to yield four cross-correlation combinations for the derivation of velocities for each cluster target. We required that each target yield a minimum of two satisfactory cross-correlations with peak values $CC \geq 0.3$ to qualify as a successful result (a result of $CC = 1$ would indicate a perfect correlation). A mean of the cross-correlation results, weighted by the associated Tonry & Davis R-value and corrected for solar motion, was used to calculate heliocentric radial velocities for a total of 202 M31 clusters candidates in the sample. The remainder represent:

1. Confirmed non-clusters (foreground stars, background galaxies, HII regions, open clusters etc.) identified by spectral features grossly atypical of globular clusters or radial velocities that were significantly beyond reasonable limits for the M31 GC population ($|v_{\text{obs}} - v_{\text{sys}}| > 3\sigma_v$ where $\sigma_v \sim 150 \text{ km s}^{-1}$). The status of these objects is noted in the final column of Table 3.
2. Target spectra with insufficient signal-to-noise to generate reliable velocities.
3. Seven objects with inaccurate coordinates due to misidentifications or saturation on the APM scans.

The radial velocities obtained from the WYFFOS spectra are provided in Table 3. Over half (109) of the M31 GCs for which velocities were obtained had no previously published spectroscopic data. The majority of the remaining clusters (72) had published velocities with large uncertainties of 20 – 80 km s^{-1} , and the remainder (21) had modest to high-precision velocities with errors $< 20 \text{ km s}^{-1}$. The positions of the WYFFOS targets in each of these categories are shown schematically in Figure 4.

Robust fits revealed no significant differences between the velocities determined using either template object with a given grating. A comparison of the velocities calculated for a given target from the two gratings showed only slightly larger differences; the derived velocities found using the R1200R grating data, for example, were at worst $\sim 6 \text{ km s}^{-1}$ larger than those determined from the spectra obtained using the H2400B grating. An uncertainty of $\pm 12 \text{ km s}^{-1}$ is adopted here for the M31 clusters in our sample based on the RMS

⁸Image Reduction and Analysis Facility, distributed by the National Optical Astronomical Observatories, which is operated by AURA under contract with the NSF.

of the velocity deviations for 28 targets observed in multiple fields. On average, this represents an overestimate of the true uncertainty since it incorporates certain internal systematic errors as well as statistical errors.

Figure 5 shows a comparison of those radial velocities in the present study that overlap with other samples from the literature. A linear fit, weighted by the inverse square of the published velocity uncertainties, yields $v_{\text{publ}} = 0.43 + 1.02 v_{\text{obs}} \text{ km s}^{-1}$. Overall, there is good agreement between the WYFFOS velocities derived herein and those of other studies within the adopted errors. Encouragingly, the RMS residuals of independent fits to the separate velocity samples were particularly low for the clusters which overlap with the high-precision echelle studies of Peterson (1989: $v_{\text{P89}} = -5.8 + 0.96 v_{\text{obs}} \text{ km s}^{-1}$ with $\text{RMS} = 5.7 \text{ km s}^{-1}$ for 8 objects) and Dubath & Grillmair (1997: $v_{\text{DG}} = 0.58 + 1.02 v_{\text{obs}} \text{ km s}^{-1}$ with $\text{RMS} = 8.2 \text{ km s}^{-1}$ for 5 objects). Note that the only high-precision result that deviates significantly from our fit is for B29, a cluster for which Peterson (1989) notes her velocity may be incorrect. This GC was not used in the calculation of the weighted fit or RMS, and it is circled in Figure 5.

There are two other points in Figure 5 which deviate significantly from the fit, and thus deserve mention. The open diamond above the best fit line represents the M31 globular cluster B301-S22: Barmby et al. (2000) obtained $v_r = -30 \pm 20 \text{ km s}^{-1}$, in poor agreement with the value of $-374 \pm 12 \text{ km s}^{-1}$ measured in the current study. The Barmby et al. coordinates match well with the APM coordinates for this object as provided in Table 3, so the velocity deviation does not appear to be due to a target misidentification in either study. This cluster was also measured by Federici et al. (1993), who obtained a velocity of $-419 \pm 30 \text{ km s}^{-1}$, in good agreement with the WYFFOS result. The Barmby et al. sample also had the largest RMS residuals in the comparison fits: $\text{RMS} = 110 \text{ km s}^{-1}$ for 16 objects, not including B301-S22. The reasons for this large discrepancy are not known. The open upright triangle which deviates from the fit in Figure 5 represents B109-S170, for which Huchra, Brodie, & Kent (1991) measured a velocity of $-613 \pm 24 \text{ km s}^{-1}$ (compared to $-372 \pm 12 \text{ km s}^{-1}$ from the WYF-

FOS results). Again, the coordinates for this object match well between both studies and the deviation does not appear to be due to a target misidentification.

3.2. Absorption and Reddening Corrections

Each spectrum was corrected for the effects of atmospheric absorption and for reddening in both the Milky Way and in M31 itself. Color excess values upon which the reddening calculations are based were determined using the slope (S) of the continuum between $\sim 4000 - 5000 \text{ \AA}$ as tabulated in Crampton et al. (1985), where available:

$$E_{B-V} = -0.066 S + 1.17 (B - V) - 0.32. \quad (2)$$

The slope parameter has been shown to be a good estimator of reddening, and is not very sensitive to cluster metallicity (Elson & Waltherbos 1988).

Targets with published $(B - V)$ colors but with no slope parameters or intrinsic color estimates were de-reddened to a typical color of $(B - V)_0 = 0.76$ for M31 globular clusters at large galactocentric radii (Crampton et al. 1985). Clusters with no S values (or colors) and those for which the calculated excess values were lower than a minimum foreground color excess of $E_{B-V} = 0.10$ (due to errors in the slope parameter or in the photometry) were assigned this minimum value (Frogel, Persson, & Cohen 1980; Elson & Waltherbos 1988).

3.3. Abundance Determinations

To rank the M31 clusters in the WYFFOS sample by metallicity, we have measured the strengths of various absorption features in their integrated spectra. Line indices were calculated to measure the signal in a wavelength-delineated region centered on each spectral feature relative to the signal in the blue and red continuum zones flanking the feature. In light of the fact that no flux standard star spectra were obtained during the WYFFOS observing run, it was not possible to convert photon counts directly into flux for these targets. Our motivation, however, was to obtain a metallicity ranking of the globular clusters in M31; relative flux calibration was not essential as its absence will not significantly affect narrow features and mean count ratios were used instead. Our line and continuum bandpasses were defined as shown

in Table 4 (Burstein et al. 1984; Brodie & Hanes 1986; Brodie & Huchra 1990).

Each target spectrum was shifted to zero radial velocity to define consistent line index wavelengths in the rest frame. The velocity dispersion of the M31 globular cluster system is roughly 150 km s^{-1} , a spread which translates into a nominal range of $4\sigma_v \gtrsim 600 \text{ km s}^{-1}$ in velocity. This would correspond to a wavelength shift of $\sim 9 \text{ \AA}$ at $\lambda = 4500 \text{ \AA}$, a significant fraction of the width of most of the bandpasses selected for measurement. Thus, metallicity determinations were not pursued for target spectra which had yielded no velocity cross-correlations.

The generalized feature index is defined as

$$I = -2.5 \log \left[\frac{2\bar{\mathcal{F}}_I}{\bar{\mathcal{F}}_{C1} + \bar{\mathcal{F}}_{C2}} \right] \quad (3)$$

where $\bar{\mathcal{F}}_I$, $\bar{\mathcal{F}}_{C1}$ and $\bar{\mathcal{F}}_{C2}$ represent the mean count levels in the feature bandpass and associated continuum bandpasses $C1$ and $C2$ as given by $\bar{\mathcal{F}} = (\lambda_2 - \lambda_1)^{-1} \int_{\lambda_1}^{\lambda_2} \mathcal{F} d\lambda$ (Brodie & Hanes 1986; Brodie & Huchra 1990). The continuum break feature $\Delta = 2.5 \log [\bar{\mathcal{F}}_{C2}/\bar{\mathcal{F}}_{C1}]$ is a measure of the discontinuity in the continuum due to Fraunhofer line-blanketing shortward of 4000 \AA . This feature is somewhat more vulnerable to errors in the reddening and absorption corrections, as it spans a broad range in wavelength and is asymmetric.

Figure 6 shows a comparison of our line indices with published M31 globular cluster $[\text{Fe}/\text{H}]$ values from various sources (B noli et al. 1987; Huchra, Brodie, & Kent 1991; Barmby et al. 2000). The RMS differences between the line indices calculated from spectra observed in more than one field through different fibres were used to estimate the internal errors for each feature, and these are shown in the second column of Table 5. The results of linear fits in the form $LI = a + b[\text{Fe}/\text{H}]$ weighted by $1/\sigma_{[\text{Fe}/\text{H}]}$ are provided in columns 3 and 4 of Table 5. Note that only spectroscopic metallicities for overlapping targets were considered in the calibration and hence the B noli et al. (1987) near-infrared photometric metallicities were not used in the fits. In column 5 of Table 5, we provide the RMS residuals of the fit and in column 6 we list the strength of the r coefficient, a measure of the linear correlation between the line indices and published metallicities.

To best represent the metal abundances of the WYFFOS targets observed, a line index was selected to contribute to the calibration if it met the following four criteria:

1. The uncertainties associated with the line index did not exceed $\sim 20\%$ of the full range of observed values. The Fe52 index did not satisfy this condition and was thus rejected from the calibration.
2. The linear correlation coefficient r exceeded a minimum level of $r = 0.65$.
3. Numerical experimentation demonstrated that the feature strength was stable in the presence of significant changes in the adopted value of cluster reddening (e.g. in comparison with any adopted reddenings which differed from unpublished M31 values from Barmby et al. (2000)). The continuum break was found to be susceptible to reddening uncertainties and was thus rejected.
4. Only one line index that characterizes a given spectral feature was incorporated in the estimate. In the case of the magnesium triplet, the indices MgG, Mg2 and Mgb all provided an acceptable measure of essentially the same absorption feature. Of these, the Mgb index demonstrated the highest correlation coefficient and a relatively low RMS uncertainty and was therefore selected for use over the others.

Line indices which met the above criteria include the CH (G-band) feature, Mgb to characterize the strength of the magnesium b triplet, and the Fe53 iron line. Final cluster metallicities have been determined from an unweighted mean of the $[\text{Fe}/\text{H}]$ values calculated from the CH(G), Mgb and Fe53 line strengths for 202 of the WYFFOS targets. These metallicities and their associated errors are provided in columns 7 and 8 of Table 3. A plot of the correlation between our $[\text{Fe}/\text{H}]$ values and those in other samples from the literature is presented in Figure 7. The best-fit of the data in Figure 7 has a slope of 0.94 ± 0.02 and the RMS of the fit residuals is 0.24. The median value of the formal errors on our WYFFOS metallicities is ± 0.26 dex.

3.4. The Best Current Sample

In the subsequent analysis, our results were merged with the velocities and $[\text{Fe}/\text{H}]$ values from other sources in order to produce the best available sample of spectroscopic data. Wherever data from other publications overlapped with our WYFFOS sample *and* demonstrated smaller associated uncertainties, these data superseded the WYFFOS results; such cases are noted in the final column of Table 3. In this final sample, 191 WYFFOS velocities and 189 metallicities were combined with data from Peterson (1989), Huchra, Brodie, & Kent (1991), Federici et al. (1993), Dubath & Grillmair (1997), and Barmby et al. (2000) to yield a total M31 globular cluster spectroscopic database comprising 321 velocities and 301 metallicities.

Barmby et al. (2000) identify the following targets as having spectral properties which are inconsistent with globular clusters: B55-S116 (stellar), B308 (galaxy), B341-S81 (stellar) and B392-S329 (stellar). We concur with the identification of B308 as a definite non-cluster and with that of B392-S329 as a probable non-cluster, and do not carry these through the remainder of the analysis. We do not find any clear abnormalities in the spectra of the other targets and thus cannot at present reject these as confirmed non-clusters.

In an effort to verify that there are no obvious biases in the metallicity sample studied here, we examine the color distribution of our sample and compare it to that of the overall M31 GCS. The mean estimated intrinsic color of 412 M31 globular clusters with $(B - V)$ data from Barmby et al. (2000) was $(B - V)_0 = 0.67 \pm 0.04$, while that for the sample of those with $[\text{Fe}/\text{H}]$ values used in the metallicity analysis presented herein (264 clusters with colors) was determined to be $(B - V)_0 = 0.65 \pm 0.05$. Based on this and a comparison of the color histograms for the metallicity sample and the overall GCS (Figure 8), we conclude that there are no significant population biases with respect to the color of the metallicity sample presented herein. A Kolmogorov-Smirnov two-sample test on the distributions in Figure 8 confirms what the eye suggests: the color distribution of the metallicity sample is drawn from the same parent population as the overall color sample at a high confidence level (99.5%).

Clearly, the globular clusters at small galacto-

centric radii will suffer from more severe effects of incompleteness due to obscuration by the disk and bulge of M31. Depending on the color/metallicity distribution as a function of position within the galaxy, this observational effect will conceivably bias the observed metallicity sample. We will return to this point in Section 4.1.

4. M31 Cluster Metallicities

The metal abundance properties of M31's globular clusters are of interest as they bespeak the galaxy's formative processes and enrichment history. The metallicity distribution for the M31 GCS is presented in Figure 9, along with a similar plot for the Milky Way GCS for comparison. The mean metallicity of the full complement of 301 M31 globular clusters is $[\text{Fe}/\text{H}] = -1.21 \pm 0.03$, comparable to the value of -1.27 ± 0.05 obtained for the Milky Way GCS (based on data supplied in Harris (1996), revised 1999). However, a Kolmogorov-Smirnov test reveals that the Galactic and M31 globular clusters have $[\text{Fe}/\text{H}]$ distributions which are drawn from the same parent population at only the 55% confidence level.

As is frequently the case with binned data, the appearance of the histogram can be ambiguous and potentially misleading, and thus a more robust method of analysis is desirable. In order to examine the shape of the metallicity distribution without relying on binning methods, we turned to the KMM algorithm used by Ashman, Bird, & Zepf (1994). KMM mixture modeling operates under the assumption that the data is independently drawn from a parent population which consists of a mixture of N Gaussian distributions. The KMM test has previously been applied to the M31 globular cluster metallicity distribution by Ashman & Bird (1993), albeit with a significantly smaller data sample.

A bimodal distribution was tested against the assumption of a unimodal shape (the null hypothesis) for the GCS metallicities. Since there is no obvious reason to assume that both $[\text{Fe}/\text{H}]$ groups in a bimodal fit would exhibit a common covariance, heteroscedastic fitting was applied such that the covariances for the two distributions were not constrained to be identical. The KMM results revealed that this 2-group fit demonstrated a marginal improvement over a single group fit,

although Ashman, Bird, & Zepf (1994) cautioned that the output probability in the heteroscedastic case is more difficult to interpret and may, in and of itself, be suspect. We repeated the KMM test on more than 1500 simulations with bootstrap resampling and found that the bimodal case was preferred over the unimodal distribution at a median confidence level of higher than 97%. The bimodal test returned Gaussian fits characterized by means at $[\text{Fe}/\text{H}] = -1.44$ ($\sigma^2 = 0.22$) for the metal-poor distribution and at $[\text{Fe}/\text{H}] = -0.50$ ($\sigma^2 = 0.13$) for the metal-rich clusters. The *a posteriori* probabilities of group membership returned by KMM assigned 231 clusters to the metal-poor distribution and 70 to the metal-rich population.

In their analysis, Elson & Walterbos (1988) treated the M31 GCS as comprising three distinct metallicity sub-populations: metal-poor, intermediate, and metal-rich. We employed the KMM test to ascertain whether a trimodal distribution was also consistent with the measured $[\text{Fe}/\text{H}]$ values for the M31 cluster system. The trimodal KMM results with bootstrap resampling demonstrated that a 3-group fit was indeed preferred over a single Gaussian distribution at a relatively high confidence level (96%). The output population means obtained for the best 3-group fit were located at $[\text{Fe}/\text{H}] = -1.59$ ($\sigma^2 = 0.19$), -1.18 ($\sigma^2 = 0.18$) and -0.47 ($\sigma^2 = 0.12$). The numbers of clusters assigned to each group were $N = 153, 76$ and 72 , respectively.

In light of the variation in the magnitude of $[\text{Fe}/\text{H}]$ uncertainties quoted within the WYFFOS sample and others, it is appropriate to test the effects of these uncertainties on the inferred shape of the distribution. There are 229 GCs with metallicity uncertainties lower than 0.45 dex, a value roughly equal to the variance of one of the populations as determined from the bimodal results. We applied the KMM test to this higher-precision sample to test the stability of our earlier conclusions. The bimodal case was again found to represent a statistically significant improvement over the unimodal assumption with peaks similar to those found when we incorporated the complete sample. The input assumption of three peaks, however, did not return adequate fits: the *a posteriori* probabilities of group membership in the trimodal case allocated only two clusters to the intermediate population.

There is an unavoidable smearing of the metallicity distribution due to metallicity calibration uncertainties, absorption and reddening of bulge/disk clusters and other line-of-sight problems, or errors incurred as a result of combining different datasets. As a further test, simulations were run in which we shuffled the high-precision $[\text{Fe}/\text{H}]$ sample by a random fraction of their associated uncertainties. This returned a result of marginal significance (median p-value ~ 0.1) for the 2-group case, and an insignificant result (p-value ~ 0.4) for the 3-group heteroscedastic trial. Note that the shapes of the 2-group Gaussian fits were once again consistent with those of the original bimodal test using the full sample.

In light of these KMM results, we tentatively reject the possibility of a trimodal GC metallicity distribution for the purposes of the analysis which follows. While it may yet be reasonable to separate the cluster system into more than two populations — say, by culling out the intermediate targets with group membership probabilities between 0.4 and 0.6 in the bimodal case — we elect not to do so here, as it is not clear that these represent a *bona fide* intermediate population. Based on the available data, we argue that the metallicity distribution of the M31 globular cluster system is not unimodal and better resembles a bimodal distribution similar in general shape to that of the Milky Way (Zinn 1985). Therefore, “metal-poor” and “metal-rich” populations shall refer to those objects separated into two groups based on the *a posteriori* probabilities returned from the 2-group heteroscedastic KMM test with the complete available sample. Each population was independently fit using an adaptive kernel smoothing procedure⁹ and the results are shown in Figure 10.

The positions of our adopted metallicity peaks ($[\text{Fe}/\text{H}] = -1.44$ and -0.50) differ only slightly from those quoted by Barmby et al. (2000), who found a bimodal distribution in M31 GC metallicities and metallicity-sensitive colors with peaks at $[\text{Fe}/\text{H}] = -1.4$ and -0.6 . Our peaks are also similar to the values of $[\text{Fe}/\text{H}] = -1.5$ and -0.6 obtained by Ashman & Bird (1993) using the KMM test on an earlier sample of 144 M31 globular clusters; their study yielded a ratio of metal-rich to

⁹Adaptive kernel smoothing code kindly provided by Karl Gebhardt.

metal-poor globular clusters of 49:95, in comparison with a ratio of 70:231 found in the current study.

4.1. Spatial Distribution

The projected spatial distributions of the metal-poor and metal-rich cluster populations are shown in Figure 11. The metal-rich population is clearly more centrally concentrated, an effect which has been demonstrated previously with a smaller dataset (Huchra, Brodie, & Kent 1991). In the Milky Way, the metal-rich clusters have been ascribed as belonging to a thick disk system (Zinn 1985; Elson & Walterbos 1988; Armandroff 1989). Later work has suggested that this is better described as a bulge/bar cluster system (Minniti 1995; Côté 1999; Forbes, Brodie & Larsen 2001). The spatial concentration and distribution of the metal-rich clusters in M31 appear to be consistent with the latter interpretation.

There is a notable deficit of metal-poor clusters in the innermost radial bins shown in Figure 12. The already strong central concentration in the metal-rich population might mask any analogous deficit in this population. A similar lack of central clusters was reported by Elson & Walterbos (1988) within the inner 15' of the GCS and is at least partially attributable to sampling restrictions towards the middle of the galaxy, as well as to observational biases incurred as a result of obscuration by the bulge and disk. The cluster sample at large galactocentric radii is bound to be more complete at faint magnitudes due to the lower degree of absorption as compared with the inner cluster system.

Examination of Figure 13 reveals a modest lack of clusters fainter than $V \approx 17$ within the inner 10' or so of the GCS. We attempt to estimate the incompleteness at small radii in the following manner. Using available V photometry (Barmby et al. 2000), we plot the observed luminosity functions (LFs) for the metal-rich and metal-poor clusters beyond a galactocentric radius of 15'. These outer LFs are normalized to the same scale as the distributions within the inner 15' by summing under the brighter end of the inner and outer histograms ($V < 16.75$ mag) and multiplying by the ratio of these values. The observed histograms for the inner metal-rich and metal-poor clusters are shown by the solid lines in Figure 14, and the scaled

outer histograms are represented by the dotted lines. Note that this method provides only a very crude estimate of the number of missing clusters at $V \geq 16.75$ as it presumes, perhaps falsely, that the shape of the globular cluster LF does not change within the inner region of the galaxy. Dynamical destruction will have a more severe effect on the inner clusters and will thus change the overall shape of the luminosity function. Evidence for this effect has previously been noted by Kavelaars & Hanes (1997).

From the scaled outer LFs in Figure 14, we infer that there are possibly ~ 30 missing metal-poor clusters at $V \geq 16.75$, whereas there may be only ~ 8 faint, metal-rich clusters which are missing within the inner 15' of the galaxy. Therefore, sample incompleteness is a reasonable explanation for the dip in the central bins of the metal-poor radial profile.

Comparing simple counts of the cluster populations within quadrants centered on the major and minor axes reveals that there is a slight enhancement in the minor axis fields for the metal-rich population: 40 clusters in the East-West sectors versus 30 in the North-South. If one takes into account only the inner 30' of the GCS, this enhancement largely vanishes for the metal-rich clusters: 28 clusters are found within the major axis sectors compared to 26 along the minor axis. Based on their photometric metallicity estimates, Elson & Walterbos (1988) discovered that their sample of clusters classified as metal-rich defines a flattened system with an ellipticity of $\epsilon \gtrsim 0.4$ within a major axis radius of 30'. Our cluster counts are not consistent with such a large degree of flattening of the metal-rich system in this region. At present, we cannot provide reasonable limits on the flattening of the metal-poor cluster distribution, since the arrangement of the WYFFOS fields has resulted in a selection bias in favor of clusters in major axis sectors at radii beyond $\sim 30'$.

4.2. Metallicity Gradient

Several previous works have suggested the presence of a weak metallicity gradient in the M31 cluster system out to radii of ~ 10 kpc (Sharov 1988; Huchra, Brodie, & Kent 1991). In Figure 15, we plot the metallicity of the M31 globular clusters as a function of galactocentric radius for the full sample and the separate metallicity sub-

populations. The large scatter in these plots is due at least in part to the fact that we can only measure projected positions, but nonetheless we find that the mean $[\text{Fe}/\text{H}]$ does indeed decrease with radius.

A sliding bin method was used to fit the mean metallicity in $12'$ bins centered on each data point, with results shown in Figure 15. Robust estimates of the mean metallicity in radial bins are consistent with the presence of a modest gradient in $[\text{Fe}/\text{H}]$ within the full sample. Separating the data into sub-populations reveals no clear evidence for a gradient in the metal-rich GCS, although the spread in metallicity does seem to increase towards the center of the galaxy. There is an apparent trend towards decreasing metallicity within both the full sample and the inner metal-poor cluster system, with gradients of roughly -0.017 and -0.015 dex/arcmin, respectively. Relatively poor sampling of the clusters at large radii makes it difficult to comment decisively on the results beyond a radius of about $60'$, although the metal-poor sample appears to level off at a lower mean metallicity beyond this distance.

5. GCS Kinematics

The maximum likelihood value for the mean cluster radial velocity is $\langle v \rangle = -284 \pm 9 \text{ km s}^{-1}$, somewhat higher than M31's systemic velocity of $-300 \pm 4 \text{ km s}^{-1}$ (RC3). The globular clusters have an overall velocity dispersion of $\sigma_v = 156 \pm 6 \text{ km s}^{-1}$. The kinematics of metal-rich and metal-poor GCS populations will be discussed later in this section. First, we examine the global kinematic properties of the M31 GCS.

5.1. GCS Rotation

A histogram of the cluster line-of-sight velocities is presented in Figure 16. There is strong evidence for bimodality in the velocity distribution, a feature which is attributable to the fact that the cluster system is rotating with respect to our line of sight. Considering, for the moment, a purely rotating disk population of globular clusters in the reference frame of the galaxy:

$$\begin{aligned} v_{\text{GC}} &= v_{\text{rot}} \sin(i) \sin(\theta + \delta) + v_{\sigma} \\ &= v' + v_{\sigma} \end{aligned} \quad (4)$$

where v_{rot} is the rotation velocity of the population, i is the inclination of the rotation axis to the line of sight (77.7°), θ is the angle about the angular momentum axis, δ is an arbitrary phase offset, and v_{σ} incorporates the velocity dispersion plus random measurement errors. The combined probability distribution $P(v_{\text{GC}})$ for the M31 globular cluster radial velocities is the convolution of $P(v')$ with $P(v_{\sigma})$. The probability distribution $P(v_{\sigma})$ is Gaussian and $P(\theta)$ is uniform, thus $P(v')$ is given by:

$$\begin{aligned} P(v') &= P(\theta) \frac{d\theta}{dv'} \\ &= \frac{1}{2\pi} \frac{1}{\sqrt{v_{\text{rot}}^2 \sin^2 i - v'^2}}. \end{aligned} \quad (5)$$

This represents a bimodal distribution with maxima at $\pm v_{\text{rot}} \sin(i)$ about the systemic velocity of the population. The peaks of the (unshifted) velocity histogram in Figure 16 lie at -415 and -170 km s^{-1} , yielding an estimated rotation amplitude of $v_{\text{rot}} \sim 125 \text{ km s}^{-1}$.

The fact that M31 is rotating has been established by various studies (see Hodge 1992, and references therein). Using a sample of ~ 150 M31 clusters as dynamical tracers, Huchra, Brodie, & Kent (1991) noted a rapid rotation of the handful of inner ($R \lesssim 7'$) clusters in their sample with $[\text{Fe}/\text{H}] \geq -0.8$ (see also Huchra, Stauffer, & Van Speybroeck (1982)). Huchra, Brodie, & Kent (1991) discovered that the metal-poor population had no rotation signature within the inner galaxy, but shared a moderate rotation of $\sim 60 \text{ km s}^{-1}$ with the bulk of the GCS beyond this radius. With our increased sample of 321 velocities, we can now provide a more comprehensive look at the kinematics of the M31 globular cluster system.

Perhaps not surprisingly, there appears to be no significant rotation of the GCS about the major axis of M31 as shown in the left panel of Figure 17. A robust fit to the targets within the inner $50'$ along the minor axis (dropping 11 objects at large radii) gives $v_r = -286 + 0.13 Y \text{ km s}^{-1}$, where Y is the distance along the minor axis in arcminutes. Such a small deviation from a slope of zero may simply be due to statistical imprecision or variation in the position angle for the galaxy (Hodge & Kennicutt 1982).

A plot of the observed cluster radial velocities

as a function of projected distance along the major axis of M31 is shown in the right panel of Figure 17. A basic 2σ culled robust linear fit to the velocities along the major axis reveals that the globular cluster system indeed has a significant rotational component about the minor axis. This rotation will now be investigated in more detail.

We used an adaptive binning technique to generate the GCS rotation curve shown in Figure 18. Before fitting the rotation curve, the globular cluster coordinates were transformed into the reference frame of the galaxy and the data were folded about each axis. The function $v = v_{\text{sys}} + v_{\text{rot}} \sin \phi$ was fit to the radial velocities of the clusters within radial bins outwards from the galaxy center (Kissler-Patig & Gebhardt 1998). The angle ϕ represents the position angle of the target object in the projected frame of the galaxy, and v_{sys} is the mean velocity of the cluster system. The kinematic properties were determined in a series of annuli centered on each cluster and encompassing a specified number of data points (79 points, with a minimum of 39 at the extrema). With this method, we obtain a rotation amplitude of 136 km s^{-1} where the curve flattens off beyond $R = 30'$.

We then employed the robust biweight estimators of location and scale (Beers, Flynn, & Gebhardt 1990; Hoaglin, Mosteller, & Tukey 2000) as measures of mean velocity and dispersion in 10 arcminute bins along the major axis of the galaxy. The biweight results and their 90% confidence intervals (based on bootstrap errors) are presented in Figure 19 for the full sample and the two metallicity sub-populations. Based on the appearance of these plots, it seems reasonable to approximate the shape of the curve as consisting of solid-body rotation within the central $25'$, with a flattening beyond this radius. One-half of the velocity difference between the flat regions of the curve in Figure 19 yields a rotation amplitude of $v_{\text{rot}} = 138 \pm 13 \text{ km s}^{-1}$ for the full sample.

Significant differences between the kinematic properties of the metal-rich and metal-poor clusters may indicate that these populations underwent dissimilar formation mechanisms. The maximum likelihood value for the mean velocity of the 70 clusters in the metal-rich sample is $\langle v \rangle = -260 \pm 18 \text{ km s}^{-1}$ with a dispersion of $\sigma_v = 146 \pm 12 \text{ km s}^{-1}$. For comparison, the larger metal-poor

sample of 231 clusters demonstrates a somewhat lower mean velocity of $\langle v \rangle = -290 \pm 10 \text{ km s}^{-1}$ and a slightly higher dispersion of $\sigma_v = 155 \pm 7 \text{ km s}^{-1}$, although these values are still consistent with those of the higher metallicity sample within the quoted errors. From the fits of the biweight results, we determine a rotation amplitude of $v_{\text{rot}} = 160 \pm 19 \text{ km s}^{-1}$ for the metal-rich population. This value is somewhat larger than the metal-poor amplitude of $v_{\text{rot}} = 131 \pm 13 \text{ km s}^{-1}$, although these values are also not inconsistent within their formal errors.

For each cluster, the projected position angle was determined as the angle of maximum positive rotation obtained from the maximum likelihood sinusoid fits (Kissler-Patig & Gebhardt 1998). Plots of the variation of position angle with radius for the full sample and metallicity sub-populations are presented in Figure 20. The input GC positions already incorporate a de-rotation of $\text{PA}_{\text{M31}} = 38^\circ$ for the galaxy and, all else being equal, one would expect to find that the PA for the cluster system is roughly zero. Despite the sizeable spread at low radius in the full sample, there is a relatively clear increase in PA within the central region of the metal-poor cluster system. This effect is consistent with studies of the central bulge and inner disk region of M31 which demonstrate a similar increase in PA (Hodge & Kennicutt 1982; Kent 1989). The M31 GCS shows a notable decrease in the PA of the rotation axis beyond about $30'$. Interestingly, the metal-rich clusters seem to be rotating about an axis that is tilted at a slightly lower PA with respect to the major axis throughout the full radial extent of the population.

5.2. The Mass of M31

The kinematics of M31's GCS provide us with a dynamical probe of the underlying mass distribution of the host galaxy (Federici et al. 1990, 1993). The projected mass estimator (PME) was used to place constraints on the underlying mass of the system (Bahcall & Tremaine 1981; Heisler, Tremaine, & Bahcall 1985):

$$M_{\text{PME}} = \frac{f_p}{NG} \sum_{i=1}^N r_i v_i^2, \quad (6)$$

where N is the number of bodies, G is the gravitational constant, r is the projected galactocentric

radius and v is the radial velocity of the body relative to the systemic velocity of the galaxy. The factor f_p depends on the assumptions made regarding the distribution of orbits, and is equal to $32/\pi$ and $64/\pi$ for isotropic and radial orbits, respectively.

Admittedly, this projected mass estimate is hampered by our limited sample size and coverage, as well as a lack of detailed understanding of the cluster orbits. Recent work by Evans & Wilkinson (2000) has shown that the dynamical tracers in the M31 halo exhibit a predominantly isotropic velocity dispersion. Applying the PME to the available cluster data and assuming isotropic orbits within an extended mass distribution, we estimate a mass of $M_{M31} = (4.1 \pm 0.1) \times 10^{11} M_{\odot}$ using 319 dynamical targets out to a radius of $\sim 120'$ from the galaxy center (~ 27 kpc at a distance of 770 kpc). This result is comparable to previous mass estimates obtained out to similar radii as summarized in Table 6 of Evans & Wilkinson (2000), and to the mass of $M_{M31} \sim (3.1 \pm 0.5) \times 10^{11} M_{\odot}$ found by Huchra, Brodie, & Kent (1991) based on their sample of 150 globular clusters. In the (unlikely) case of purely radial orbits, our mass estimate would be increased to twice the value quoted above.

6. Discussion and Conclusions

We have presented a sample of new spectroscopic observations of M31 globular clusters, contributing ~ 200 high-precision velocities and $[\text{Fe}/\text{H}]$ values for what represents a large fraction of the dynamical tracers of the galaxy. A comprehensive analysis of the kinematics and abundance properties of M31's GCS demonstrates some interesting similarities and differences when compared with the Milky Way's globular cluster population.

The Galactic and M31 globular cluster systems have comparable mean metallicities of $[\text{Fe}/\text{H}] \sim -1.2$ to -1.3 , although a Kolmogorov-Smirnov test provides no conclusive evidence that the two distributions are drawn from the same parent population. A KMM mixture-modeling test reveals that the M31 GCS metallicity distribution can convincingly be separated into two groups, a bimodality which is analogous to that found in the Milky Way GCS. The peaks in the M31 metallicity distribution lie at $[\text{Fe}/\text{H}] = -1.44$ and -0.50 .

A KMM test on the Milky Way GCS metallicities from the McMaster catalogue (Harris 1996) returns peaks at $[\text{Fe}/\text{H}] = -1.59$ and -0.56 , indicating that the metal-poor Galactic globulars have, on average, a somewhat lower metal abundance than their M31 counterparts. Of the 301 M31 globular clusters with available metallicities, KMM assigns 70 to the metal-rich peak. This represents a somewhat smaller fraction of high-metallicity clusters than is found in the Milky Way system, for which 45 of 145 are identified with the metal-rich population.

M31's metal-rich globular clusters appear to constitute a distinct kinematic subsystem that is quite spatially concentrated, consistent with membership in a bulge population akin to the inner metal-rich clusters of the Milky Way (Minniti 1995). Furthermore, the velocity dispersion of the metal-rich cluster system, $\sigma_v = 146 \pm 12 \text{ km s}^{-1}$, is indistinguishable from the mean bulge dispersion of $\sigma_v(\text{bulge}) = 146 \pm 6 \text{ km s}^{-1}$ as determined from the kinematics of faint planetary nebulae (Lawrie 1983; van den Bergh 1991). The mean metallicity of this population is quite similar to their Milky Way counterparts and demonstrates no obvious abundance gradient with galactocentric radius. Contrary to observations in the Milky Way, however, we find no clear signs of flattening in the metal-rich component of the M31 GCS despite our relative oversampling of major axis fields in the current spectroscopic sample. We find that the rotation axis of the metal-rich cluster population is tilted at a slightly lower position angle: it is offset by about $5 - 10^\circ$ with respect to that of the minor axis of M31 and the bulk of its GCS. This observation may point to a disparate origin for these clusters. Further searches for potential cluster candidates hidden by the bulge of M31 will be helpful in providing a clearer understanding of the kinematics and nature of this inner system.

In M31, there are more than three times the number of metal-poor clusters as there are metal-rich. It is not clear if it is possible (or even necessary) to further separate this larger, more spatially distended metal-poor population into sub-components. If the metal-poor cluster distribution does indeed incorporate a thick disk component in addition to halo clusters, this would account for the relatively high net rotation amplitude and large velocity dispersion observed therein.

While grouping the clusters based on metallicity remains an instructive exercise, $[\text{Fe}/\text{H}]$ alone is not an adequate discriminator of membership in the spatially- or kinematically-defined components of the galaxy. This is primarily a result of the substantial spread and measurable gradient in $[\text{Fe}/\text{H}]$ within the metal-poor cluster system. The task of assigning globular clusters to their appropriate component (e.g. bulge, thin or thick disk, inner or outer halo) remains somewhat simpler within the Milky Way GCS, since here we have three-dimensional spatial information rather than projected positions.

We find evidence for a radial metallicity gradient (-0.015 dex/arcmin) in the metal-poor population of M31 out to about $60'$ from the galaxy center. Despite a notable lack of cluster data beyond this radius, it does seem that mean metallicity levels off, although the scatter remains large. This gradient in the metal-poor clusters is not inconsistent with a single collapse scenario, yet we recognize that a metallicity gradient, in and of itself, is not sufficient to confirm an early dissipational collapse. Such a gradient could be mimicked by a hierarchical halo formation if the metallicity of the accreting fragments correlates with their mass and mean density (Freeman 1996). The search for substructure in position/velocity/metallicity parameter space is clearly of interest to investigate the accretion history of the galaxy. An analysis of potential sub-clustering within the M31 GCS will follow in a subsequent paper.

A comprehensive investigation of the kinematics of the dynamical tracers in M31 would not be complete without the addition of planetary nebulae data. Fortunately, a study of a large sample of M31 is currently underway (Halliday et al., in preparation). Moreover, these data can be combined with the globular cluster sample to better probe the underlying mass distribution of the galaxy (Wilkinson et al., in preparation). An analysis of M31 cluster ages is also in progress (T. Bridges, private communication) which should provide a better sense of the chronology of GC formation within the galaxy. Despite its long and rich history of investigation, there is little doubt that there are missing globulars in M31's database which are awaiting discovery and identification. Continuing searches and surveys for M31 cluster candidates (Lee et al. 2001) promise to help rem-

edy this situation and to further fuel this “booming industry”. It is clear that detailed studies of the kinematics, metallicities and ages of the globular cluster systems of a large sample of galaxies can provide us with the clues necessary for a more complete understanding of the mechanisms which form and evolve galaxies of all kinds.

7. Acknowledgments

This work was supported in part by operating grants to DAH from the Natural Sciences and Engineering Research Council of Canada. JPB and JPH acknowledge funding support from the National Science Foundation. The authors wish to extend their thanks to Jim Lewis, Karl Gebhardt and Tim Beers for making their software available, and to Pauline Barmby for providing unpublished reddenings. The authors are also very grateful to the anonymous referee for the helpful comments and to the kind staff at WHT for their support during the observations.

REFERENCES

- Armandroff, T. E. 1989, *AJ*, 97, 375
- Ashman, K. M., & Bird, C. M. 1993, *AJ*, 106, 2281
- Ashman, K. M., & Zepf, S. E. 1998, *Globular Clusters* (New York: Cambridge Univ. Press)
- Ashman, K. M., Bird, C. M., & Zepf, S. E. 1994, *AJ*, 108, 2348
- Baade, W., & Arp, H. 1964, *ApJ*, 139, 1027
- Bahcall, J. N., & Tremaine, S. 1981, *ApJ*, 244, 805
- Barmby, P., Huchra, J. P., Brodie, J. P., Forbes, D. A., Schroder, L. L., & Grillmair, C. J. 2000, *AJ*, 119, 727
- Battistini, P., Bònoli, F., Braccési, A., Fusi Pecci, F., & Malagnini, M. L. 1980, *A&AS*, 42, 357
- Battistini, P., Bònoli, F., Braccési, A., Federici, L., Fusi Pecci, F., Marano, B., & Börngen, F. 1987, *A&AS*, 67, 447
- Battistini, P. L., Bònoli, F., Casavecchia, M., Ciotti, L., Federici, L., & Fusi Pecci, F. 1993, *A&A*, 272, 77

- Beers, T. C., Flynn, K., & Gebhardt, K. 1990, *AJ*, 100, 32
- Bònoli, F., Delpino, F., Federici, L., & Fusi Pecci, F. 1987, *A&A*, 187, 25
- Bridges, T. J. 1998, in *Fibre Optics in Astronomy III*, ASP Conf. Ser. 152, eds. S. Arribas, E. Mediavilla and F. Watson, 104
- Brodie, J. P., & Hanes, D. A. 1986, *ApJ*, 300, 258
- Brodie, J. P., & Huchra, J.P. 1990, *ApJ*, 362, 503
- Burstein, D., Faber, S., Gaskell, M., & Krumm, N. 1984, *ApJ*, 287, 586
- Cole, S., Lacey, C. G., Baugh, C. M., & Frenk, C. S. 2000, *MNRAS*, 319, 168
- Côté, P. 1999, *AJ*, 118, 406
- Côté, P., Marzke, R. O., & West, M. J. 1998, *ApJ*, 501, 554
- Crampton, D., Cowley, A. P., Schade, D., Chayer, P. 1985, *ApJ*, 288, 494
- de Vaucouleurs, G., de Vaucouleurs, A., Corwin Jr., H.G., Buta, R. J., Paturel, G., & Fouque, P., Third Reference Catalogue of Bright Galaxies, 1991, Version 3.9 (RC3)
- Dubath, P., & Grillmair, C. J. 1997 *A&A*, 321, 379
- Eggen, O. J., Lynden-Bell, D., & Sandage, A. R. 1962, *ApJ*, 136, 748
- Elson, R. A. W., & Walterbos, R. A. M. 1988, *ApJ*, 333, 594
- Evans, N. W., & Wilkinson, M.I. 2000, *MNRAS*, 316, 929
- Federici, L., Fusi Pecci, F., & Marano, B. 1990, *A&A*, 236, 99
- Federici, L., Bònoli, F., Ciotti, L., Fusi Pecci, F., Marano, B., Lipovetsky, V. A., Neizvestny, S. I., & Spassova, N. 1993, *A&A*, 274, 87
- Forbes, D. A., Brodie, J. P., & Grillmair, C. J. 1997, *AJ*, 113, 1652
- Forbes, D. A., Brodie, J. P., & Larsen, S. S. 2001, *ApJ*, 556, L83
- Freeman, K. C. 1996, in *Formation of the Galactic Halo...Inside and Out*, ASP Conf. Ser. 92, eds. H. Morrison and A. Sarajedini, 3
- Frogel, J. A., Persson, S. E., & Cohen, J. G. 1980, *ApJ*, 240, 785
- Harris, W. E. 1996, *AJ*, 112, 1487 (McMaster catalogue, revised June 1999) <http://physun.physics.mcmaster.ca/Globular.html>
- Heisler, J., Tremaine, S., & Bahcall, J. N. 1985, *ApJ*, 298, 8
- Hoaglin, D. C., Mosteller, F. & Tukey, J. 2000, *Understanding Robust and Exploratory Data Analysis* (New York: Wiley & Sons)
- Hodge, P. 1992, *The Andromeda Galaxy*, (Dordrecht: Kluwer), Ch. 7
- Hodge, P. W., & Kennicutt, R. C. 1982, *AJ*, 87, 264
- Hubble, E. 1932, *ApJ*, 76, 44
- Huchra, J. P., Stauffer, J., & Van Speybroeck, L. 1982, *ApJ*, 259, L57
- Huchra, J. P., Brodie, J. P., & Kent, S. M. 1991, *ApJ*, 370, 495
- Kavelaars, J., & Hanes, D. A. 1997, *MNRAS*, 285, 31
- Kent, S. 1989, *AJ*, 97, 1614
- Kissler-Patig, M., & Gebhardt, K. 1998, *AJ*, 116, 2237
- Lawrie, D. G. 1983, *ApJ*, 273, 562
- Lee, M. G., Kim, S. C., Geisler, D., Seguel, J., Sarajedini, A., & Harris, W. E. 2001, in *Extragalactic Star Clusters*, IAU Symp. Ser. 207, eds. E. Grebel, D. Geisler, and D. Minniti, in press
- Minniti, D. 1995, *AJ*, 109, 1663
- Parmentier, G., Jehin, E., Magain, P., Noels, A., & Thoul, A. A. 2000, *A&A*, 363, 526
- Peterson, R. 1989, in *Dynamics of Dense Stellar Systems*, ed. D. Merritt (Cambridge: Cambridge Univ. Press), 161

Rosenberg, A., Saviane, I., Piotto, G., & Aparicio, A. 1999, AJ, 118, 2306

Rubin, V. C., & Ford, W. K. Jr. 1970, ApJ, 159, 379.

Saito, Y. & Iye, M. 2000, ApJ, 535, L95

Sargent, W. L. W., Kowal, C. T., Hartwick, F. D. A., & van den Bergh, S. 1977, AJ, 82, 947

Sarajedini, A., Chaboyer, B., & Demarque, P. 1997, PASP, 109, 1321

Searle, L., & Zinn, R. 1978, ApJ, 225, 357

Sharov, A. S. 1988, SvA, 14, L339

Sommer-Larsen, J., Beers, T. C., Flynn, C. Wilhelm, R. & Christensen, P. R. 1997, ApJ, 481, 775

Stetson, P. B., Bolte, M., Harris, W. E., Hesser, J. E., van den Bergh, S., VandenBerg, D. A., Bell, R. A., Johnson, J. A., Bond, H. E., Fullton, L. K., Fahlman, G. G., & Richer, H. B. 1999, AJ, 117, 247

Tonry, J., & Davis, M. 1979, AJ, 84, 1511

van den Bergh, S. 1969, ApJS, 171, 145

van den Bergh, S. 1991, PASP, 103, 1053

Vetešnik, M. 1962, BAC, 13, 180

Zepf, S. E., & Ashman, K. M. 1993, MNRAS, 264, 611.

Zinn, R. 1985, ApJ, 293, 424

TABLE 1
TARGET CATALOGUE REFERENCES

Code	Reference
B	Battistini et al. (1980, 1987)
S	Sargent et al. (1977)
BA	Baade & Arp (1964)
BoD	Battistini et al. (1987) Table VI
DAO	Crampton et al. (1985)
NB	Battistini et al. (1993)
V	Vetešnik (1962)

TABLE 2
OBSERVING LOG

Field ID	α_{B1950}	δ_{B1950}	Night	UT	Exp (Sec)	Grating
Central 1	00:40:00.18	+40:59:59.9	Nov. 3/4	21:00	6×1800	H2400B
Central 1	00:40:00.43	+41:00:00.5	Nov. 3/4	00:43	3×1200	R1200R
Northeast 1	00:42:29.88	+41:36:02.0	Nov. 4/5	21:52	6×1800	H2400B
Northeast 1	00:42:29.88	+41:36:01.1	Nov. 4/5	01:22	3×1200	R1200R
Southwest 1	00:37:30.15	+40:24:01.7	Nov. 5/6	19:32	3×1200	R1200R
Southwest 1	00:37:30.51	+40:24:00.0	Nov. 5/6	20:42	4×1800	H2400B
Northeast 2	00:44:59.97	+42:11:53.4	Nov. 5/6	23:43	5×1800	H2400B
Northeast 2	00:45:00.70	+42:11:56.3	Nov. 5/6	02:40	3×1200	R1200R
Central 2	00:39:59.20	+41:00:05.2	Nov. 6/7	19:26	3×1200	R1200R
Central 2	00:39:59.34	+41:00:03.7	Nov. 6/7	20:38	4×1800	H2400B
Southwest 2	00:34:59.80	+39:47:54.6	Nov. 6/7	23:33	5×1800	H2400B
Southwest 2	00:35:00.56	+39:47:54.6	Nov. 6/7	02:25	4×1200	R1200R

TABLE 3
WYFFOS RESULTS

GC	RA (B1950)	Dec (B1950)	X (')	Y (')	v (km s ⁻¹)	[Fe/H]	Notes
(Complete table available in published version)							

TABLE 4
LINE INDICES AND COLORS

Index	C1	I	C2
HK	3910.00 – 3925.00	3925.00 – 3995.00	3995.00 – 4015.00
CNR	4082.00 – 4118.50	4144.00 – 4177.50	4246.00 – 4284.75
CaI	4200.00 – 4215.00	4215.00 – 4245.00	4245.00 – 4260.00
CH(G)	4268.25 – 4283.25	4283.25 – 4317.00	4320.75 – 4335.75
Δ	3800.00 – 4000.00	...	4000.00 – 4200.00
H β	4829.50 – 4848.25	4849.50 – 4877.00	4878.25 – 4892.00
MgH	4897.00 – 4958.25	5071.00 – 5134.75	5303.00 – 5366.75
Mg2	4897.00 – 4958.25	5156.00 – 5197.25	5303.00 – 5366.75
MgG	5125.00 – 5150.00	5150.00 – 5195.00	5195.00 – 5220.00
Mgb	5144.50 – 5162.00	5162.00 – 5193.25	5193.25 – 5207.00
Fe52	5235.50 – 5249.25	5248.00 – 5286.75	5288.00 – 5319.25
Fe53	5307.25 – 5317.25	5314.75 – 5353.50	5356.00 – 5364.75

TABLE 5
CORRELATION BETWEEN LINE INDICES AND [Fe/H]

Line	σ	a	b	RMS	r
H&K	0.10	0.51	0.16	0.12	0.37
CNR	0.06	0.18	0.11	0.08	0.51
CaI	0.06	0.00	-0.01	0.06	-0.05
CH(G)*	0.08	0.25	0.09	0.06	0.68
Δ	0.20	1.31	0.24	0.14	0.70
H β	0.02	0.03	-0.05	0.05	-0.34
MgH	0.04	0.13	0.02	0.04	0.52
Mg2	0.05	0.20	0.11	0.05	0.72
MgG	0.03	0.13	0.06	0.02	0.75
Mgb*	0.04	0.20	0.09	0.03	0.80
Fe52	0.04	0.11	0.05	0.02	0.61
Fe53*	0.03	0.09	0.04	0.02	0.66

NOTE.—Features marked with an asterisk were used in the final [Fe/H] calibration.

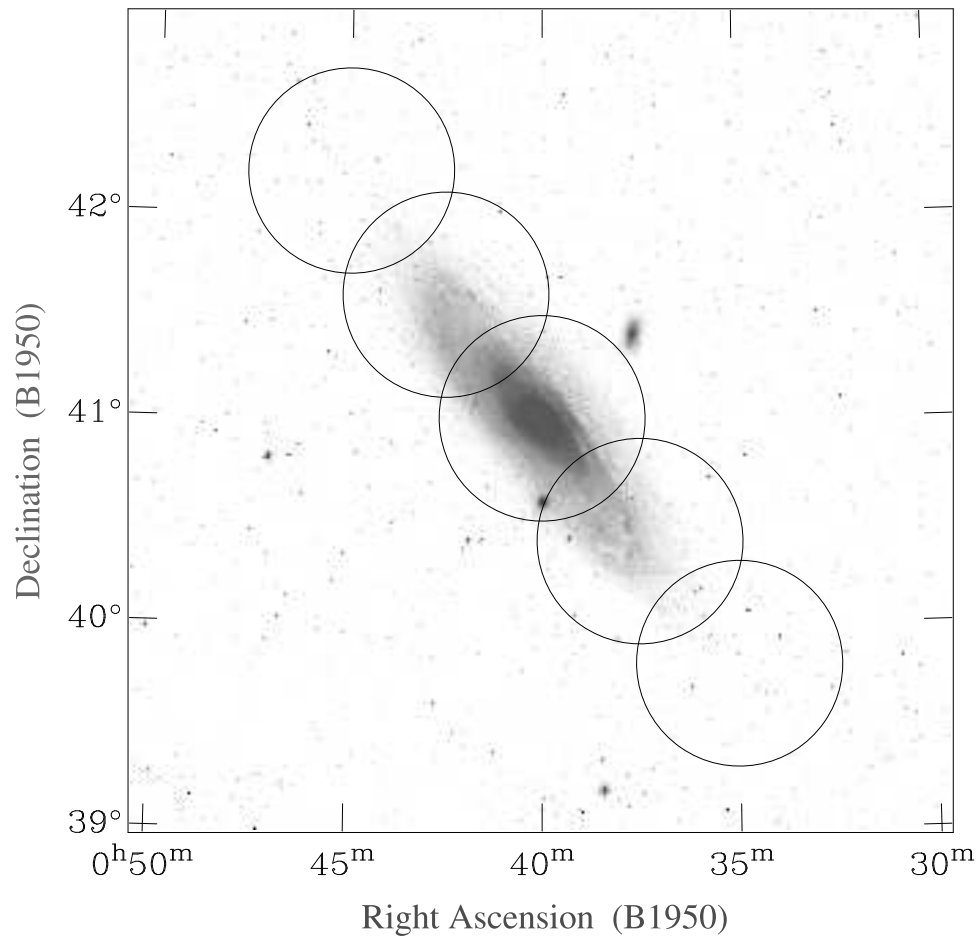


Fig. 1.— Five 1° WYFFOS fields shown superimposed over an optical image of the galaxy from the Digitized Sky Survey. Two central fibre configurations were used to yield spectral observations for a total of 288 cluster candidates. North is to the top, east is towards the left.

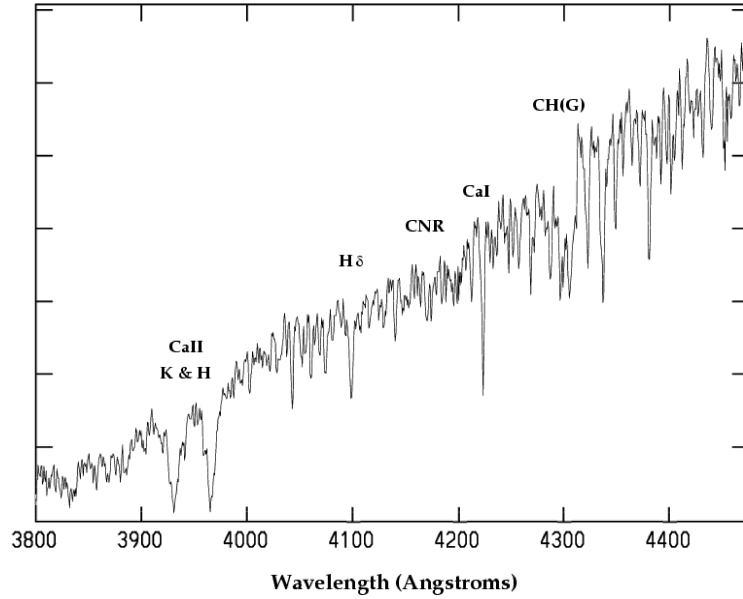


Fig. 2.— A sample reduced spectrum for M31 globular cluster B19, obtained using the WYFFOS system and the H2400B grating. The ordinate axis is linear in arbitrary units (zero counts is at the bottom).

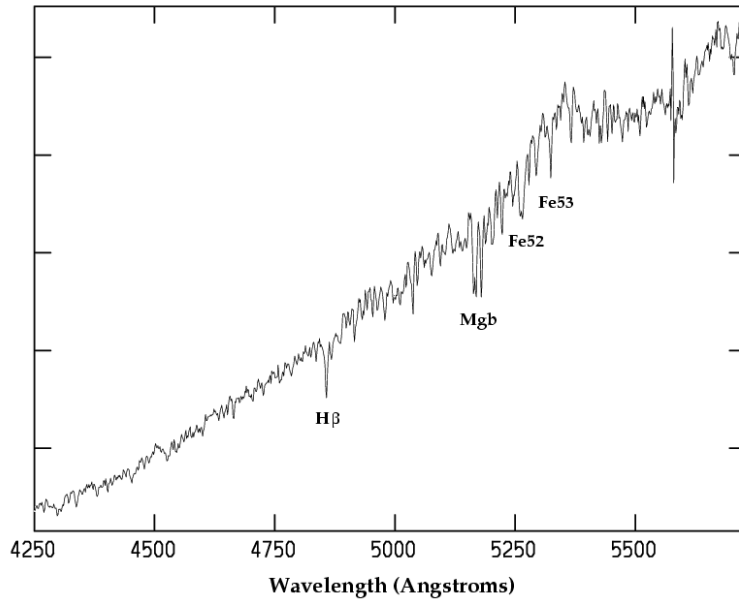


Fig. 3.— A sample reduced spectrum for M31 globular cluster B19 obtained using the WYFFOS system and the R1200R grating. The ordinate axis is linear in arbitrary units (zero counts is at the bottom).

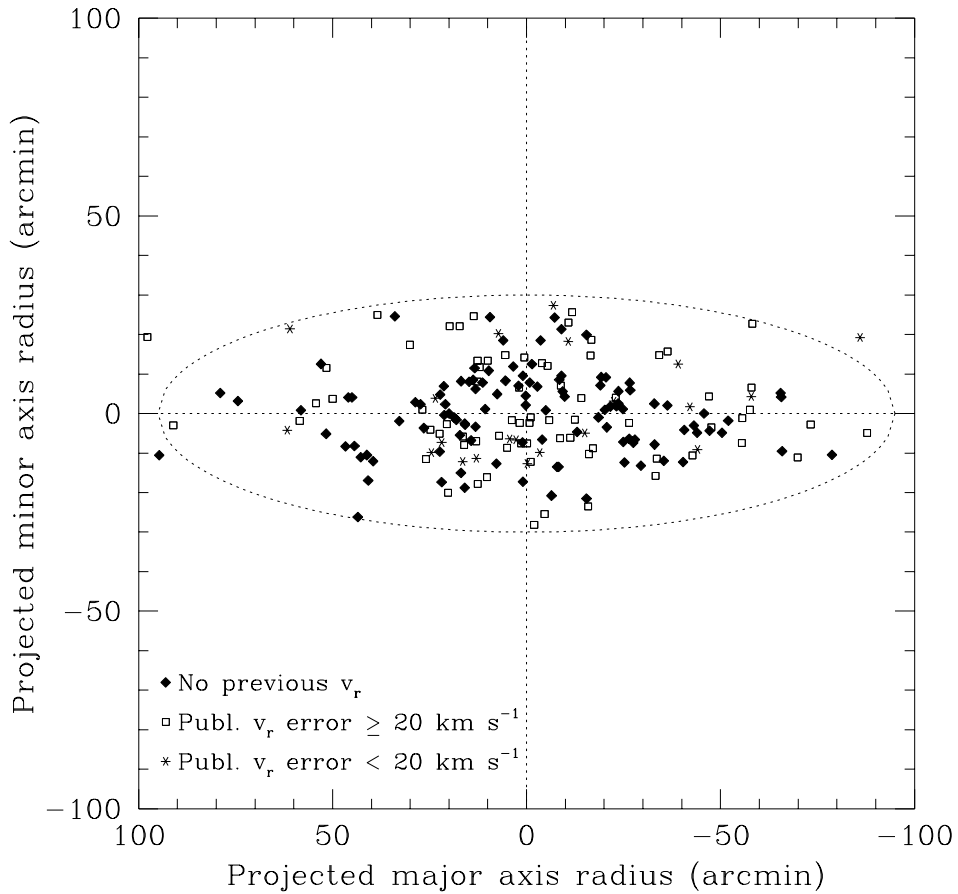


Fig. 4.— The positions of the 202 M31 GCs for which radial velocities were obtained from the WYFFOS spectra. Over half of this sample had no previously published spectroscopic data. Of those that had, our velocities (with adopted uncertainties of $\pm 12 \text{ km s}^{-1}$) represent significant improvements over most of the pre-existing spectroscopic data.

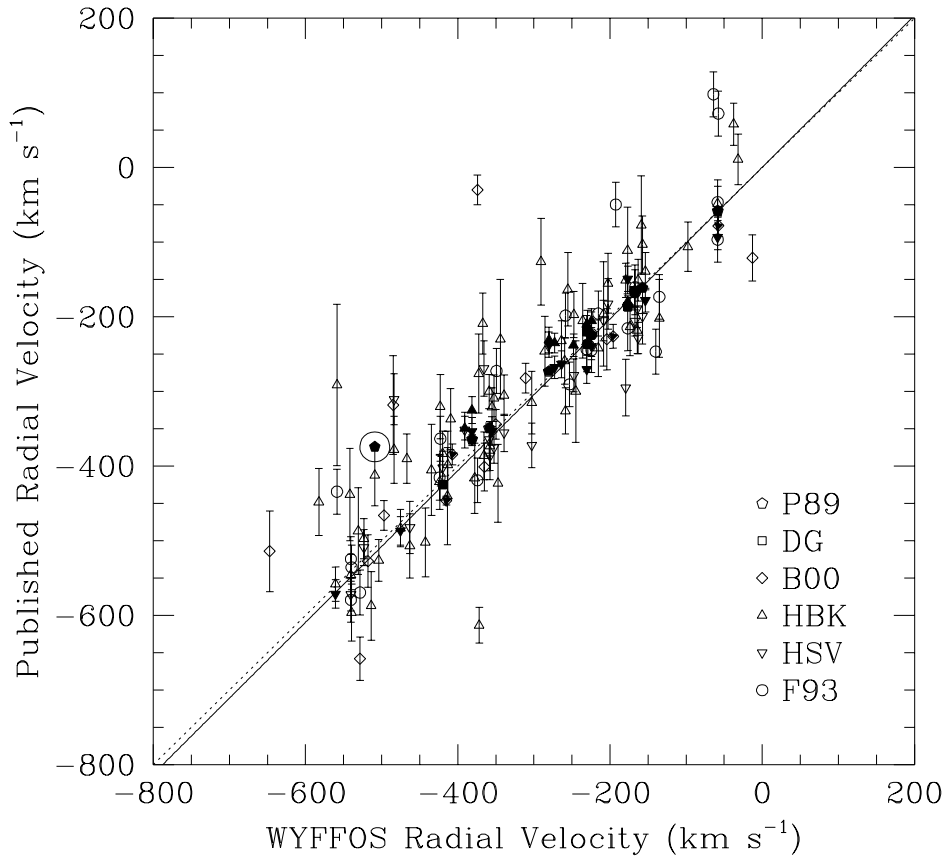


Fig. 5.— A comparison between radial velocity results obtained from this study and those in other publications: P89 = Peterson (1989); DG = Dubath & Grillmair (1997); B00 = Barmby et al. (2000); HBK = Huchra, Brodie, & Kent (1991); HSV = Huchra, Stauffer, & Van Speybroeck (1982); F93 = Federici et al. (1993). Filled points represent high-precision velocity determinations with quoted errors less than 20 km s^{-1} . The unity relation is represented by the dotted line, and the results of a linear fit with a $1/\sigma^2$ weighting is shown by the solid line. The circled (filled) point is M31 globular cluster B29 (see text for details).

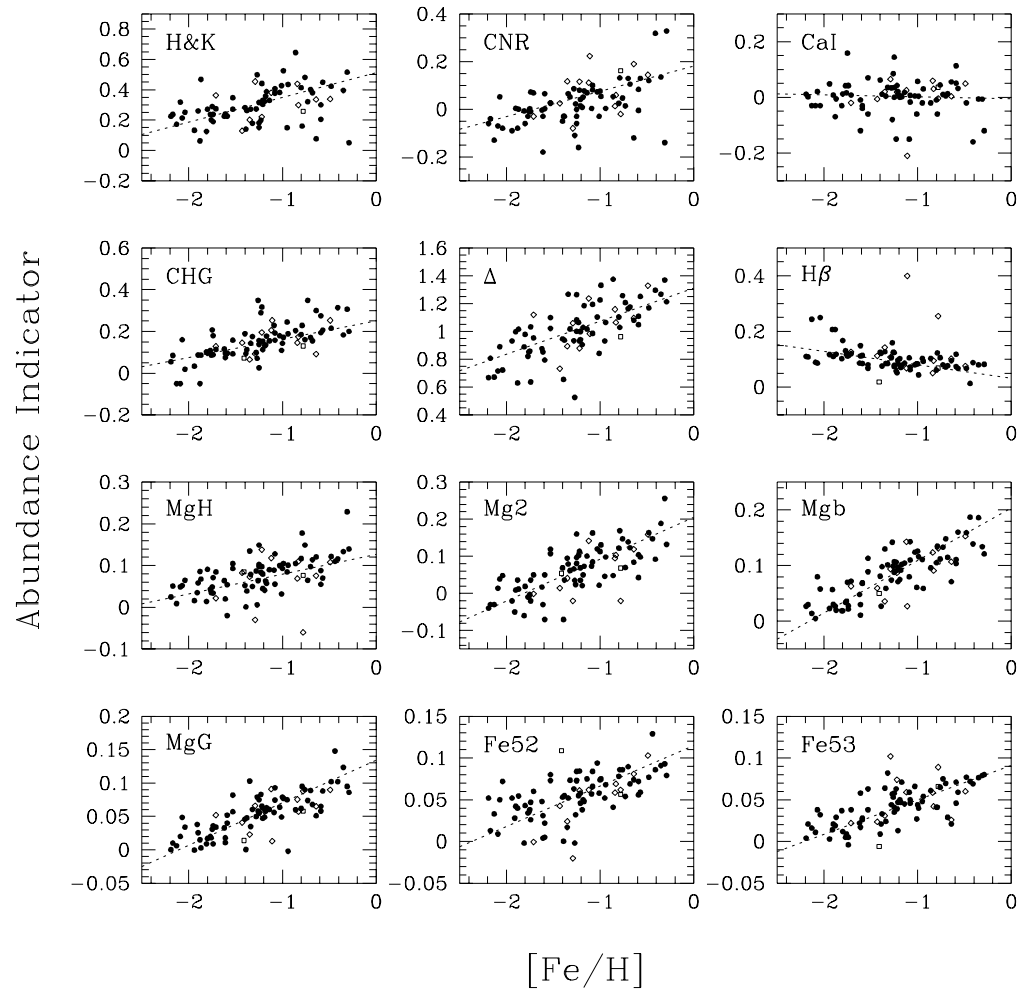


Fig. 6.— The relationship between published line $[\text{Fe}/\text{H}]$ values and the line indices in this study. Metallicity sources are as follows: ● Huchra et al 1991, ◇ Barmby et al 2000 and □ Bònoli et al 1987. The dotted lines represent linear fits to the data, weighted by $1/\sigma_{[\text{Fe}/\text{H}]}^2$.

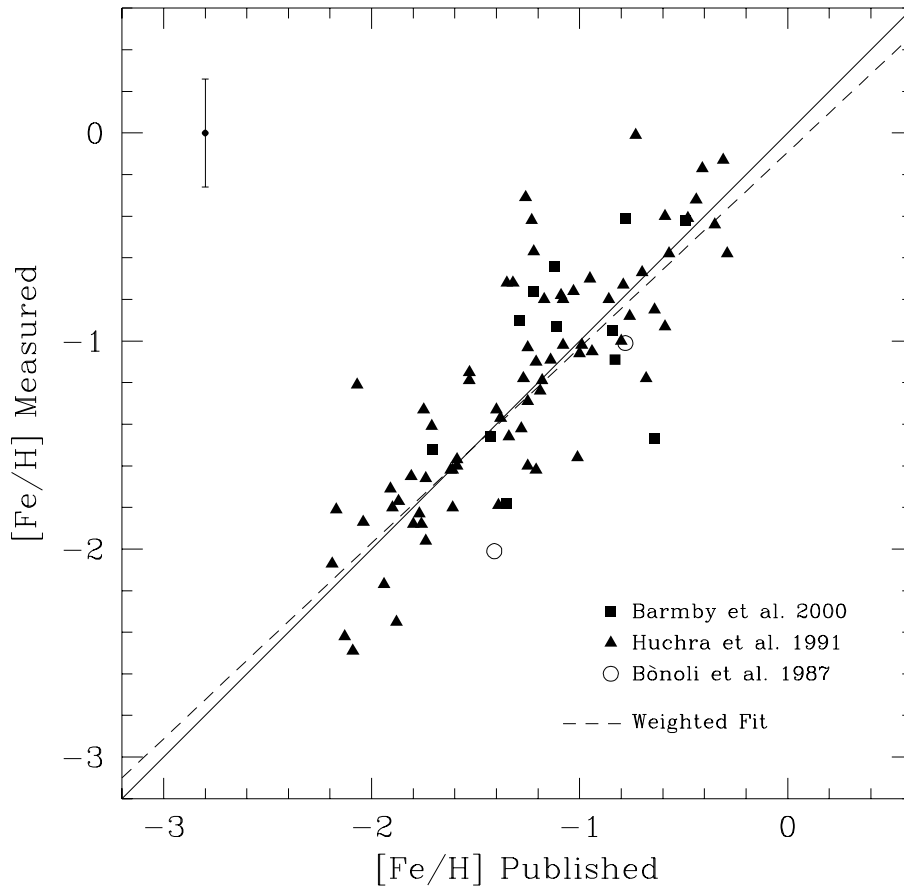


Fig. 7.— The relationship between published line $[\text{Fe}/\text{H}]$ values and the calibrated WYFFOS metallicities. The error bar in the upper left represents the median formal error quoted on the WYFFOS values. A linear fit, weighted by the inverse-square of the individual uncertainties, is shown by the dashed line for comparison to the unity relation (solid line). The slope of the fit is 0.94 ± 0.02 and the RMS of the fit residuals is 0.24 dex.

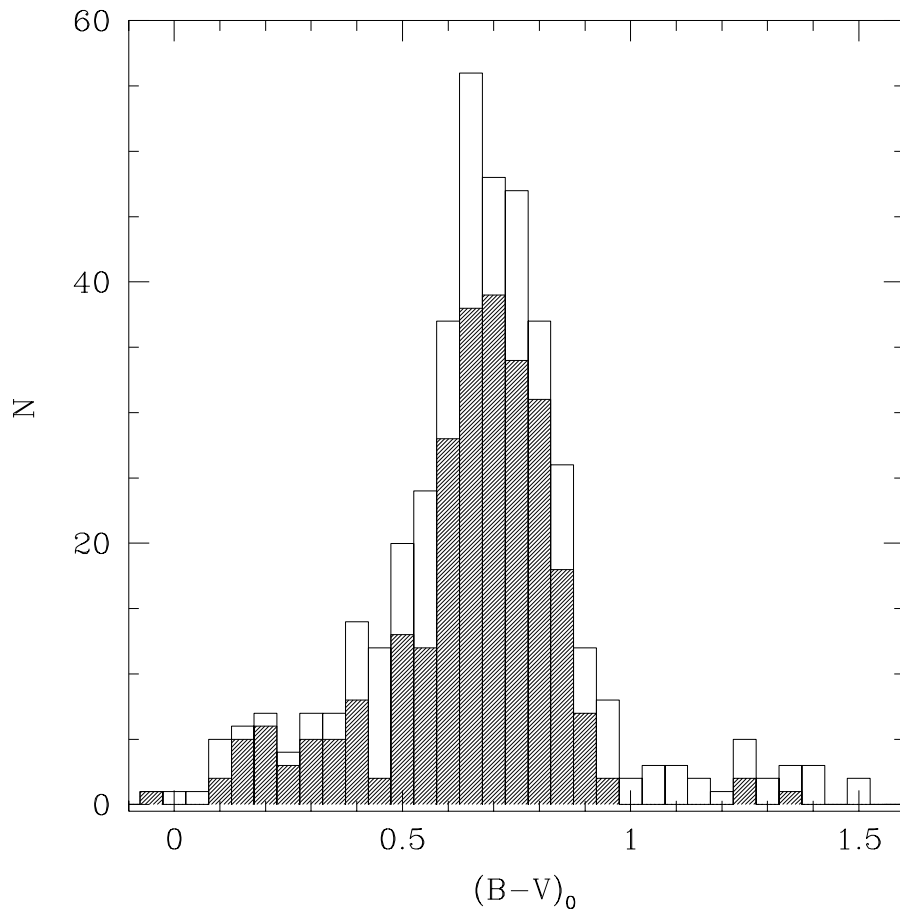


Fig. 8.— The color distribution of the M31 globular clusters for which we have spectroscopic metallicities (shaded) as compared to the overall color distribution of the GCS (solid line). There is no sign of color bias in the metallicity sample as compared to the overall M31 cluster population with available $(B - V)$ color information (from Barmby et al. 2000).

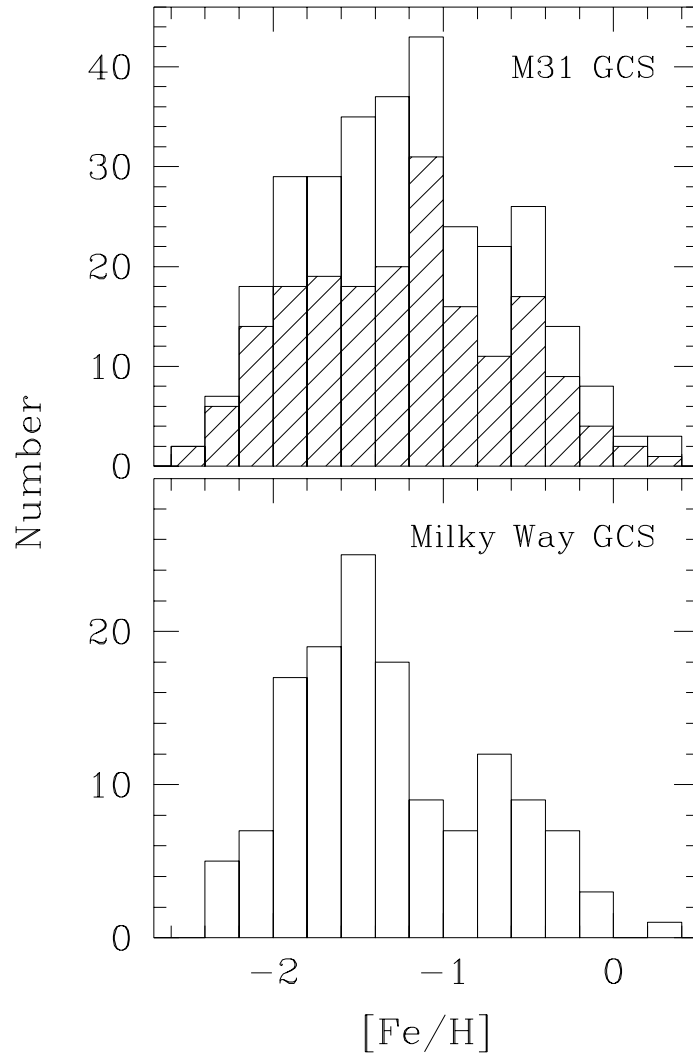


Fig. 9.— The metallicity histogram for the M31 cluster system (top) and the Milky Way GCS (bottom) for comparison. The shaded area in the top plot represents the M31 WYFFOS data.

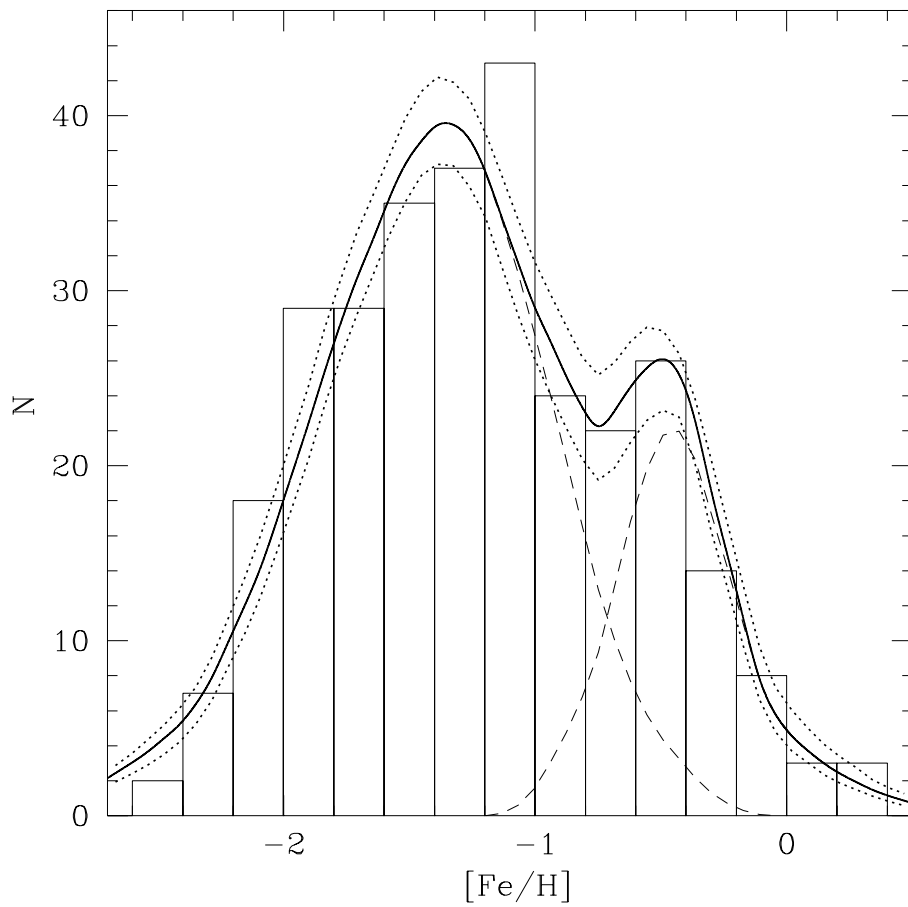


Fig. 10.— Adaptive kernel fits to the M31 metal-poor and metal-rich GC populations (dashed lines), separated according to the KMM mixture modeling results. The sum of the individual fits is shown (solid line) along with its 90% confidence interval (dotted lines).

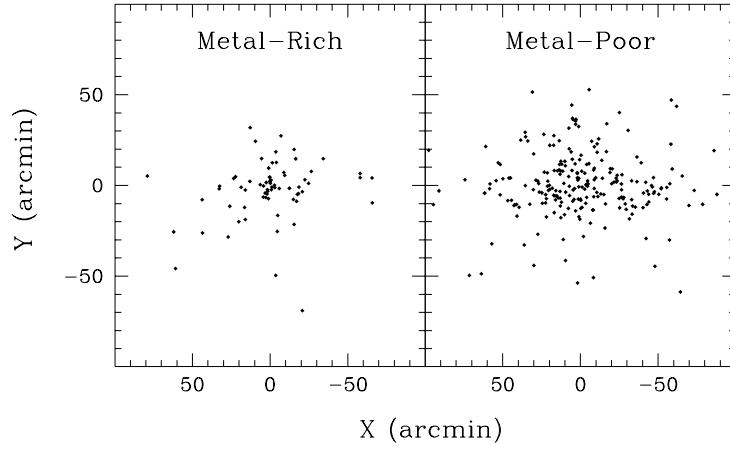


Fig. 11.— The spatial distributions of the metal-rich and metal-poor cluster populations. At an M31 distance of 770 kpc, $5'$ corresponds to just over 1 kpc.

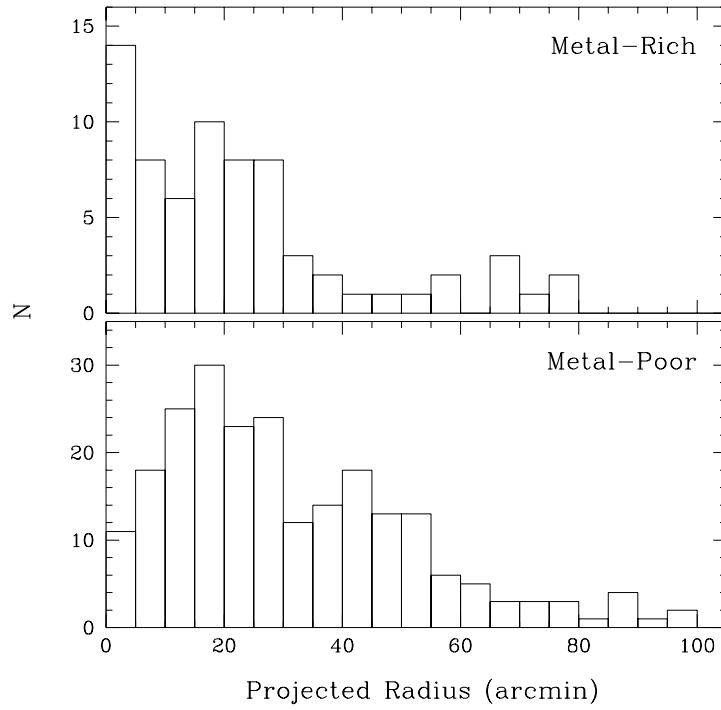


Fig. 12.— The radial distribution of M31 globular cluster populations with metallicities.

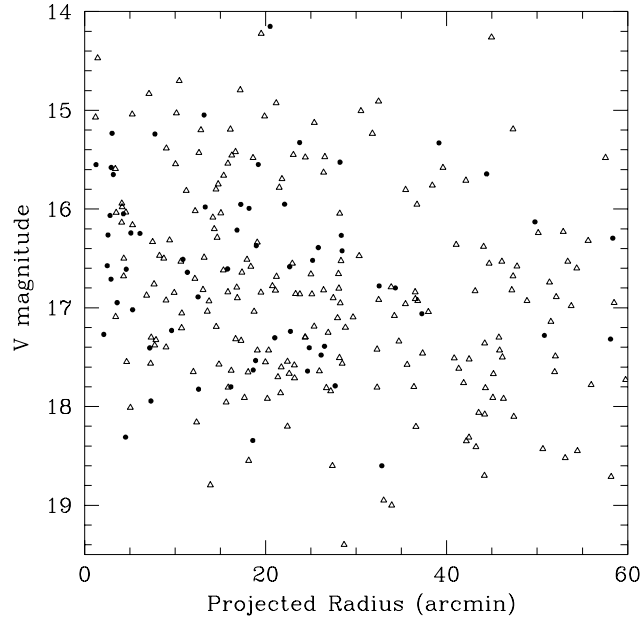


Fig. 13.— Apparent V magnitude of the clusters as a function of galactocentric radius, showing the metal-rich clusters (*filled circles*) and the metal-poor clusters (*open triangles*).

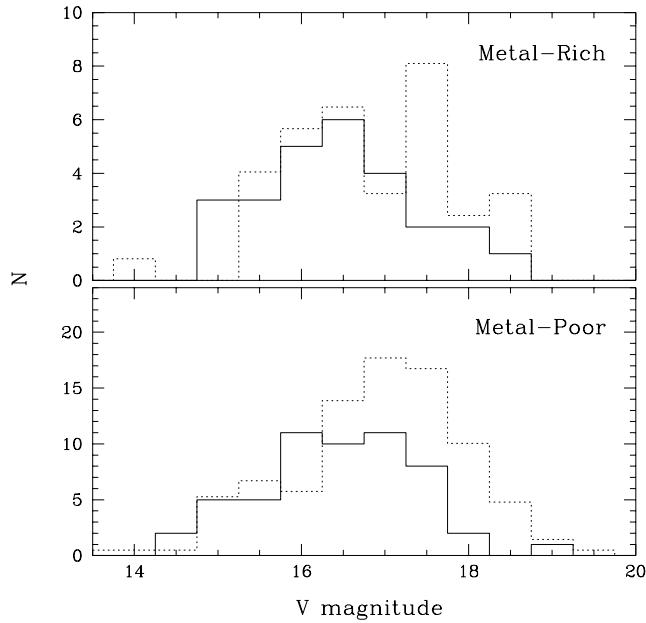


Fig. 14.— The observed luminosity functions of the metal-rich and metal-poor clusters within the inner 15' of the galaxy are represented by the solid lines. The outer cluster LFs, scaled as described in the text, are shown by the dotted lines.

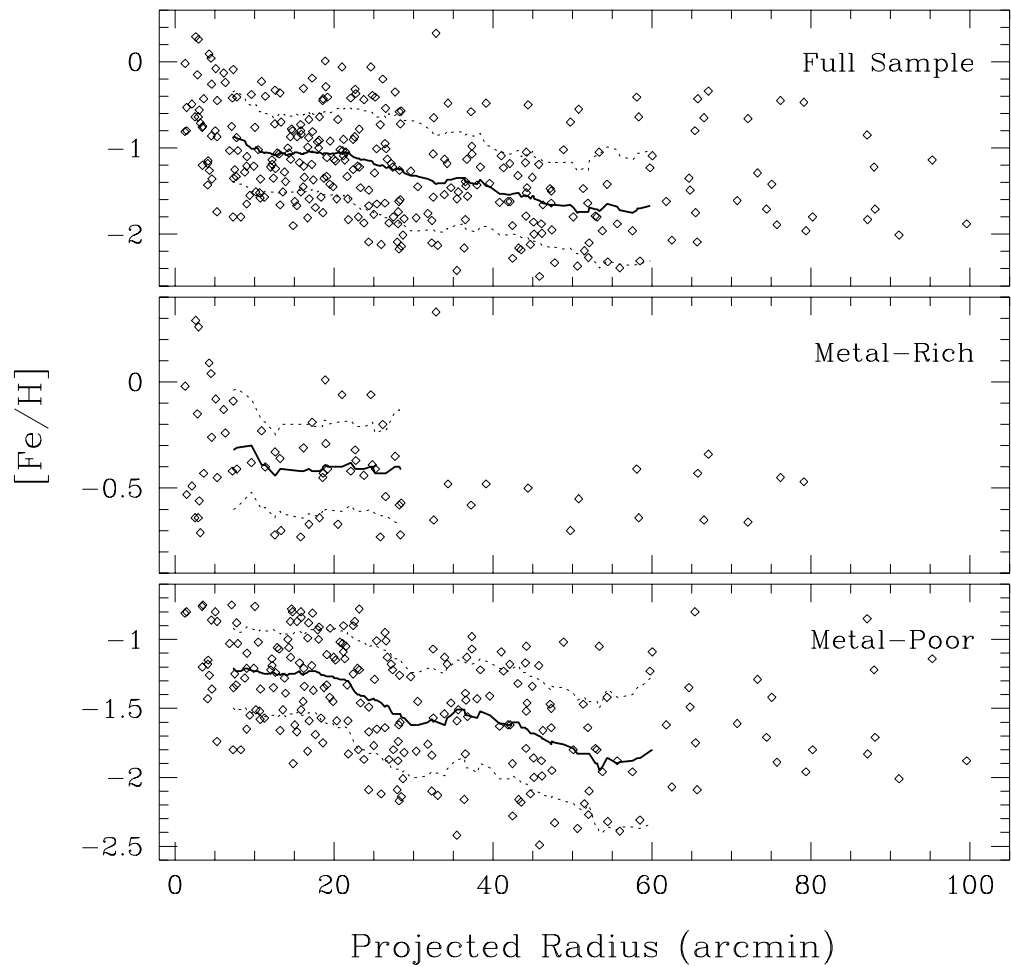


Fig. 15.— $[Fe/H]$ as a function of projected radius for the full sample and metallicity populations of the M31 GCS. A sliding-bin fit was used to determine the mean and RMS at each data point (shown by the solid and dotted curves, respectively).

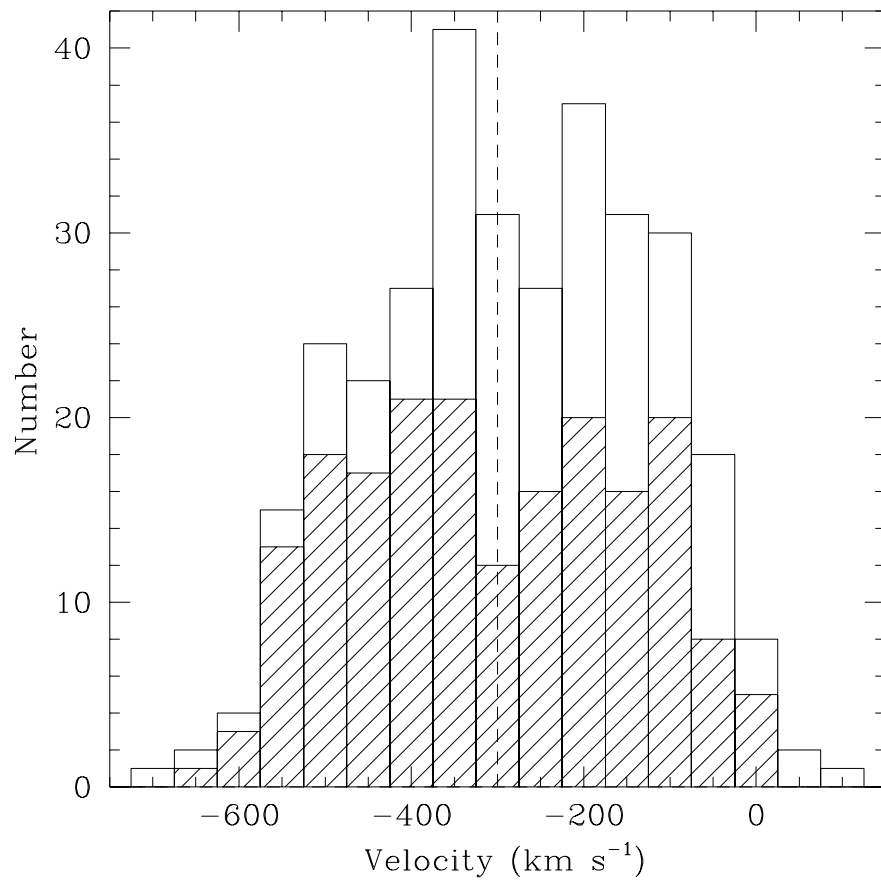


Fig. 16.— The velocity histogram for the M31 cluster system. The solid-line histogram is that for the available sample of 321 M31 globular cluster velocities, while the shaded area shows our contribution of 191 WYFFOS velocities to the overall sample. The M31 systemic velocity of $-300 \pm 4 \text{ km s}^{-1}$ is shown by the dashed line.

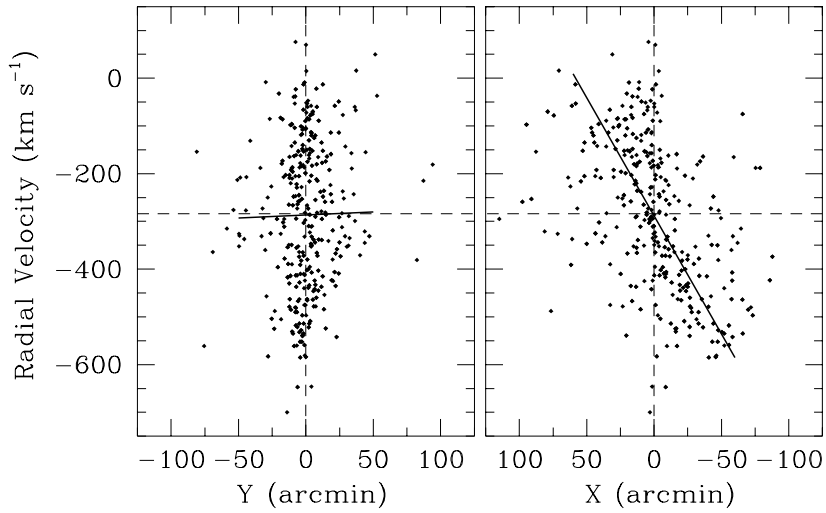


Fig. 17.— Radial velocity of the M31 globular clusters versus projected radius along the minor axis (left) and the major axis (right). Culled robust fits to the data are shown by the solid lines.

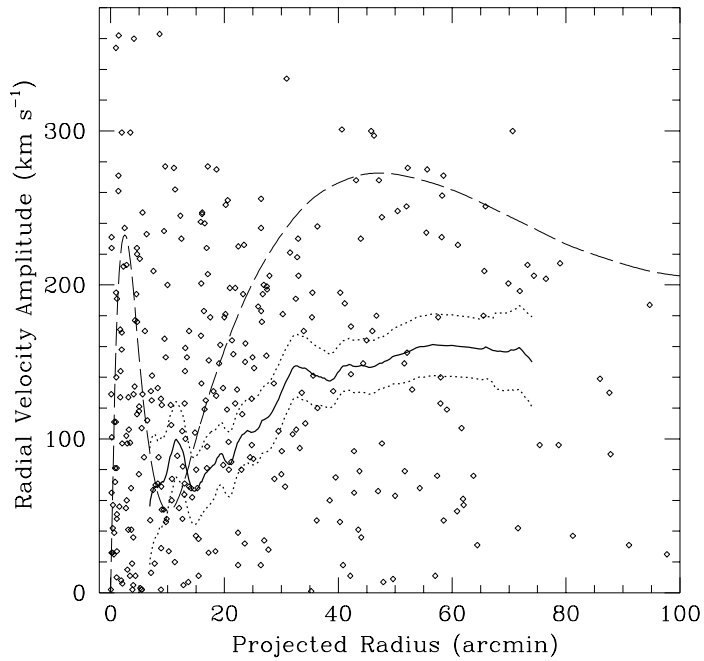


Fig. 18.— The projected rotation curve of the M31 GCS and its 90% confidence limits are shown by the solid and dotted lines, respectively (see the text for details). The dashed line represents the stellar rotation curve from Rubin & Ford (1970) for comparison.

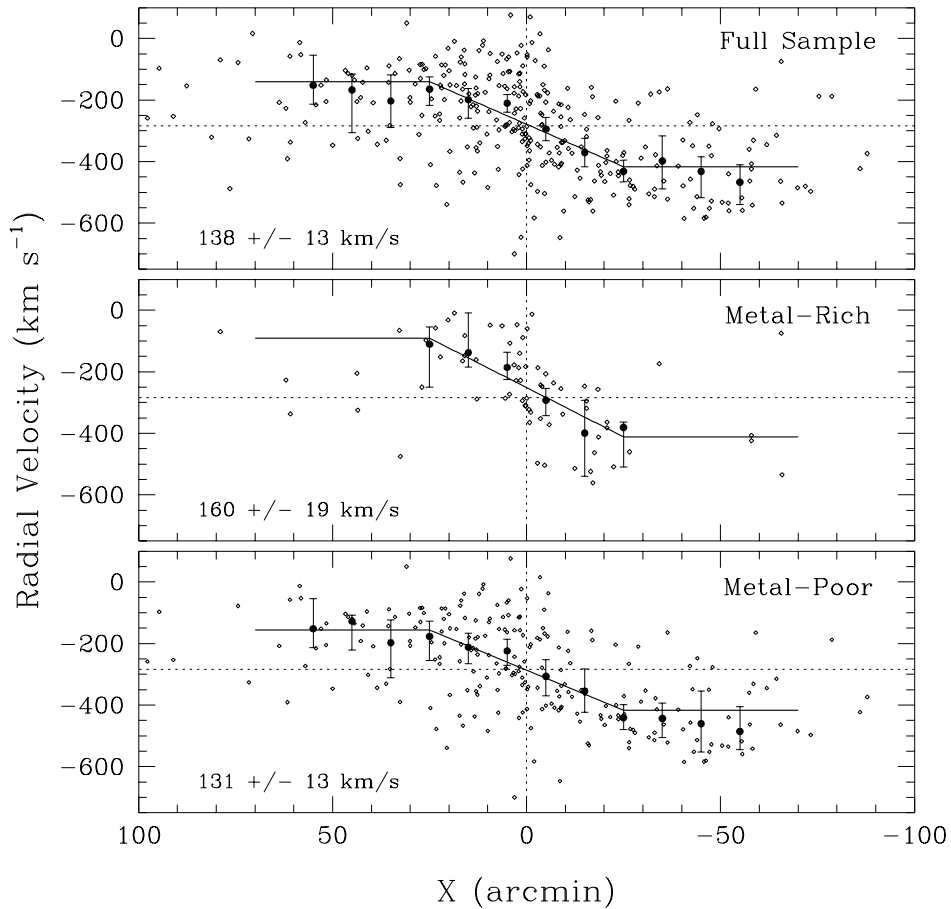


Fig. 19.— The rotation curve of the M31 GCS based on robust biweight estimates of the mean (“location”) in radial bins of 10 arcminutes for the full dataset and separate metallicity populations. The error bars represent the 90% confidence interval. The solid line shows the best fit to the data assuming solid-body rotation in the inner 25 arcminutes and flattening beyond. The derived rotation amplitudes are provided in the lower-left corner of each plot.

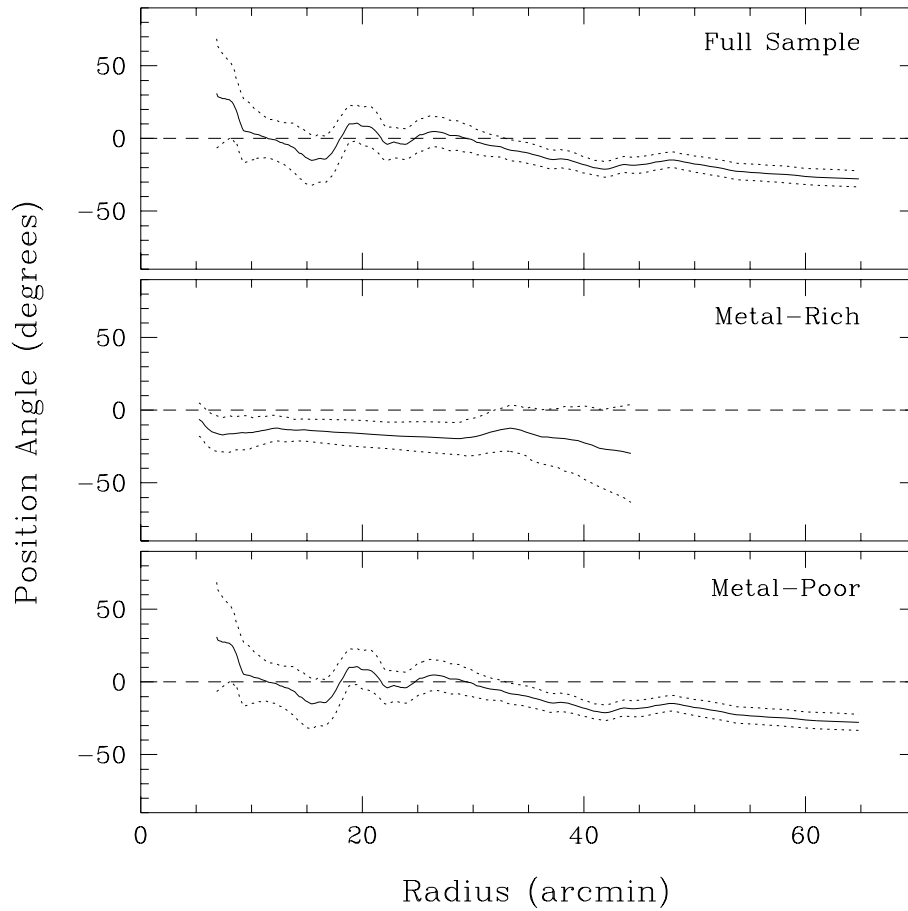


Fig. 20.— The projected position angle of the rotation axis (solid line) and its 90% confidence bands (dotted lines) as a function of radius for the full sample, as well as for the metal-rich and metal-poor populations.